RUPRECHT-KARLS-UNIVERSITÄT HEIDELBERG

Jens Appmeier

# Bose-Einstein condensates in a double well potential: A route to quantum interferometry

Diplomarbeit

HD-KIP-07-06

KIRCHHOFF-INSTITUT FÜR PHYSIK

**Faculty of Physics and Astronomy**
**University of Heidelberg**

Diploma thesis
in Physics

submitted by
**Jens Appmeier**
born in Leipzig
2007

# Bose-Einstein condensates in a double well potential: A route to quantum interferometry

This diploma thesis has been carried out by Jens Appmeier at the
Kirchhoff Institute of Physics
under the supervision of
Prof. Dr. M. K. Oberthaler

# Bose-Einstein Kondensate im Doppelmuldenpotential: Eine Möglichkeit der Quanten-Interferometrie

Im Rahmen dieser Arbeit wurde eine neue optische Dipolfalle für die BEC Apparatur unserer Gruppe geplant und aufgebaut. Der Fallenlaser hat einen minimalen Radius von $5.15\,\mu$m und ermöglicht deshalb einen starken Einschluß der Atome. Die Konzeption und der Aufbau erfolgten derart, dass der erreichbare Parameterbereich des bereits existierenden Doppelmuldenpotentials erweitert wurde. Ziel dabei war es das Fock-Regime zu erreichen. In diesem sind die Atomzahlschwankungen klein und es sollte möglich sein ein Wiederkehren der relativen Phase zwischen den beiden Mulden des Potentials zu beobachten. Dies schließt die Möglichkeit ein, unter das statistische Limit (*standard quantum limit*) der Schwankungen zu gehen und würde neue Möglichkeiten für hochgenaue interferometrische Experimente eröffnen. Infolge des starken Einschlusses der Falle werden hohe Atomdichten erreicht was zu einer hohen 3-Körper Verlustrate führt. Es wird gezeigt das es durch diesen Verlustmechanismus möglich wird die Atomzahl im Experiment sehr genau zu kontrollieren.

# Bose-Einstein condensates in a double well potential: A route to quantum interferometry

In this work a new dipole trap was designed and added to the BEC apparatus of our group. The trapping beam has a tight focus of $5.15\,\mu$m and therefore allows a strong confinement. With this new trap, the accessible parameter range of our existing double well system is expanded. The aim is to reach the Fock regime, where the relative atom number fluctuations are small and a revival of the relative phase between both lattice sites of the double well system should be observed. This includes the possibility to go beyond the *standard quantum limit* and opens new prospects for high precision interferometry experiments. Due to the strong confinement in the trap, high atomic densities can be reached. This resulted in a strong 3-body decay of the sample. As will be shown in this thesis, this loss mechanism allows to prepare a sample with a well defined atom number, in principle better than shot noise.

# Contents

# List of Figures

# Fundamental Constants

| Quantity | Symbol | Value | Unit |
|---|---|---|---|
| Speed of light | $c$ | $2.99792458 \cdot 10^{8}$ | m $s^{-1}$ |
| Boltzmann Constant | $k_B$ | $1.3806503(24) \cdot 10^{-23}$ | J $K^{-1}$ |
| Planck Constant | $h$ | $6.62606876(52) \cdot 10^{-34}$ | J s |
| | $h/2\pi$ | $1.054571596(82) \cdot 10^{-34}$ | J s |
| | $k_B/h$ | 20.836644(36) | Hz $nK^{-1}$ |
| Specific Data on Rubidium-87 | | | |
| Mass | $m$ | $1.4445 \cdot 10^{-25}$ | kg |
| s-Wave Scattering Length | $a$ | 5.32 | nm |
| Saturation Intensity | $I_{\text{sat}}$ | 1.58 | mW $cm^{-2}$ |
| D2-Line Width | $\Gamma$ | $2\pi \times 6.065$ | MHz |

# Chapter 1

# Introduction

In the year 2001 the nobel prize for physics was awarded to Eric A. Cornell, Wolfgang Ketterle and Carl E. Wieman "for the achievement of Bose-Einstein condensation in dilute gases of alkali atoms, and for early fundamental studies of the properties of the condensates" [1]. This nobel price was awarded to three of the four people who have been the first to achieve a Bose-Einstein condensate (BEC) in the year 1995.

The effect of Bose-Einstein condensation was predicted by S. Bose [2] in 1924, who devoted himself to the statistical description of the quanta of light. A. Einstein generalized this idea in 1925 to a gas of noninteracting atoms [3] with an integer spin. After the discovery of a superfluid phase in liquid helium by J. Allen and D. Misener [4], and P. Kapitza [5] in 1938 it was F. London [6, 7] who connected this phenomenon with the Bose-Einstein condensation. Only one month later L. Tisza [8] extended this model and proposed a "two-fluid" model to explain the behavior of liquid helium. One phase is the normal liquid and the second one is the superfluid fraction that consists of atoms which fall into the ground state and undergo Bose-Einstein condensation. In 1941 L. Landau [9] developed the first self-consistent theory of superfluidity.

On the experimental side it took until the 1970s for the first studies of dilute atomic gases to be developed. They benefited from the new techniques, developed in atomic physics, based on magnetic and optical trapping. This made it possible to achieve more advanced cooling mechanisms. Because of its light mass, the first studies focused on spin-polarized hydrogen to achieve Bose-Einstein condensation. It was first cooled in a dilution refrigerator, then magnetically trapped and further cooled by evaporation. But the BEC was not achieved. With the development of laser-based cooling mechanisms for neutral atoms like laser cooling and magneto-optical trapping in the 1980s the focus changed to the alkali atoms. They were well suited for those new techniques, since their optical transitions are accessible with lasers and their internal energy structure allows cooling to very low temperatures.

Combining different cooling techniques the groups of E. Cornell and C. Wieman using rubidium-87 [10], W. Ketterle using sodium-23 [11] and R. Hulet using lithium-7 [12] succeeded in 1995 to create a Bose-Einstein condensate. BEC's in other species including spin-polarized hydrogen (1998 by D. Fried *et. al* [13]) followed a little later. The observation of a BEC not only in momentum space, but also in real space opened a completely new field of research. With this technique one has a system at hand with which it is possible to study directly the quantum mechanical behavior of matter. As an example in 1997 the first interference patterns of two freely expanding condensates was

observed [14], which is a direct analog to Young's double slit experiment.

## Josephson Junction

One paradigm effect of quantum mechanics is the tunneling effect. It describes a particle passing a barrier without having enough energy for this to succeed in a classical sense. Of course, this only works if the barrier is sufficiently low, where in this context sufficiently low is still high enough to retain a particle, only familiar with the classical physics. A known example from solid state and condensed matter physics is the Josephson junction. Extensive studies of this system have been carried out using two modes of superfluid helium (see [15] for a review) or two superconductors, which are separated by a thin isolator. In a BEC one can achieve such a system by inserting a barrier into the trap and thus creating a double well system. With this, one can split a condensate into two and ends up with a similar system as in the superconductor case. What all three systems have in common is the fact, that the particles can tunnel through the barrier from one side to the other. This is because the wave functions are not strictly localized on each side of the barrier, but overlap in a small region inside the barrier leading to a tunneling of the particles. Therefor the relative phase between both wave functions is a sensible measure and can evolve in time by particles tunneling back and forth. This situation is described by a weak link.

This effect was predicted by Brian D. Josephson in 1962 [16] . He studied the behavior of two superconducting metals that are separated from each other by a barrier and predicted a tunneling current through it, which consists of Cooper-pairs. Only one year later this prediction was confirmed by P. Anderson and J. Rowell using a thin oxide layer between two superconducting metals as a weak link [17]. In 2005 the first observation of Josephson oscillations in a single Bose-Einstein Josephson junction was achieved in our group using a double well potential [18]. As the Josephson tunneling translates a phase difference between the two wells of a double well potential into an atom number difference it is well suited to build an interferometer for BEC's with this. Suppose a BEC in each well of a double well potential. At sufficiently high barrier both will evolve independently, since the tunneling between both is suppressed due to the high barrier. Each of the BEC's evolves and picks a phase. By lowering the barrier and according to this allowing Josephson tunneling between both, the relative phase will be transcribed to an atom number difference that can be detected by taking an image of the system. This is the same principle as in an interferometer, where the phase difference between both arms is transcribed into intensity differences.

## Standard-Quantum-Limit

Hence a double well potential can also be used as an atom interferometer. This is in principle the same as Young's double slit experiment, except that in this case matter waves, not light waves, do interfere.

The concept of matter waves is one of the consequences of quantum mechanics, which was developed in the 1920s. At that time several problems arose that were not consistent with the classical theory. One of these was the question if light is a wave or a stream of particles. Up to that time the opinion that light is a wave was well established. Young's

double slit experiment and the effect of Fraunhofer diffraction were clear evidences for this. With A. Einstein's explanation of the photoelectric effect in 1905 problems with this picture arose. Light seemed to have particle character. This was confirmed by the discovery of the Compton effect in 1923. L. de Broglie proposed in 1924 the wave-particle duality that states that all matter has a wavelength [19]. C. Davisson and L. Germer [20] confirmed this in 1927 by measuring the diffraction of electrons from a crystal of nickel. Before electrons were thought to be particles, because E. Rutherford showed that it is possible to guide them through the vacuum from a cathode to an anode. Quantum mechanics avoided this problem, by describing particles and waves with a (possibly complex) wave function which is the probability distribution of the considered object.

This description also yields that two conjugate variables like position and momenta (or in this case: atom number and phase) cannot be measured with arbitrarily high accuracy, but are limited to a lower boundary given by Heisenberg's uncertainty relation. In an beam splitting procedure one is also limited by the statistics underlying this process. Since the splitting of a beam into two is a Poissonian process, the uncertainty of the atom number in each of the split arms is limited to the square route of the average number $N$. This limit is denoted as the *standard quantum limit* (SQL) or *shot-noise limit* (SNL). With a quantum mechanical interferometer one can even beat this limit and approach the Heisenberg limit, which is $1/N$ [21]. This corresponds to the minimal achievable uncertainty.

## Contents of this Thesis

The present work is divided into two parts. In the first part (chapters 2 and 3) the basic theory associated to our system is explained, in addition the apparatus and the general experimental procedure to achieve a BEC is described. Chapter 2 deals with the possibility to use a double well system as a quantum interferometer and it's theoretical description using the two-mode model in two different approaches. These are the Bose-Hubbard model, where the behavior of the system is described using creation and annihilation operators and the Gross-Pitaevskii equation, a non-linear Schrödinger equation that includes the interatomic interaction. This model is used in a mean field description, where the interatomic interactions are modeled as an interaction between one particle and an effective potential, given by all the other particles. Also the relevant parameters to characterize the system depending on the trapping geometry in the outline of the new dipole trap are presented. In chapter 3 a short description of the apparatus and the steps to achieve a condensate are presented. The imaging setup and the way how to deduce the atom number and the temperature is described.

The second part consists of chapters 4 and 5, where the first one deals with the trapping properties of the new beam and the generated dipole trap. Also the optical setup is presented. In chapter 5 the first measurement benefiting from the increased confinement in the new dipole trap is presented. The three-body loss rate could be increased and a loss measurement and its theoretical description is presented. At the end of the thesis a conclusion and an outlook for further experimental work is presented.

# Chapter 2

# BEC in a double well as a quantum interferometer

With the precise control of systems of ultracold atoms it is possible to use the BEC as a measurement tool for other physical quantities. A possible application of double well systems would be the realization of an atomic gyroscope. This rotating interferometer measures the frequency of rotation very precisely using two counter propagating beams. Using this device with matter waves instead of photons can exceed it's performance by a factor of $10^4$ as it is shown in [22, 23]. Also the phase sensitivity of a standard interferometer, which is limited to $1/\sqrt{N}$ with $N$ denoting the number of particles counted, can be surpassed by matter wave interferometers using non classical states as an input to the interferometer [21].

Pure quantum effects of a double well potential should be accessible with BEC's. One example is the collapse and the revival of the relative phase between both arms of the interferometer. In a classical system the relative phase would diffuse. At no time after this process the phase would have a defined, non random value again.

In this chapter the reader will be introduced to a matter wave interferometer using BEC's in a double well potential. The aim is to get a good estimation of the atom number in the wells and their relative phase. The theoretical background will be explained and the timescale for the revival of the relative phase between both wells will be given for our setup.

## 2.1 Quantum Interferometry

The double well system can be treated as an interferometer by writing the problem in the following way, see fig. 2.1.

The atoms enter the interferometer with a wave function being normalized to the atom number $N$. The first beam splitter splits the incident beam in two. Each of them is reflected by a mirror and then both beams are overlapped again by a second beam splitter. The wave function at each path is given in the sketch of the system given in fig. 2.1.

The signal detected by detector $A$ can be derived by taking the absolute square of the wave function at that point, giving the mean atom number which will be counted there as a function of the difference of both path lengths to the detector $l_a - l_b$.

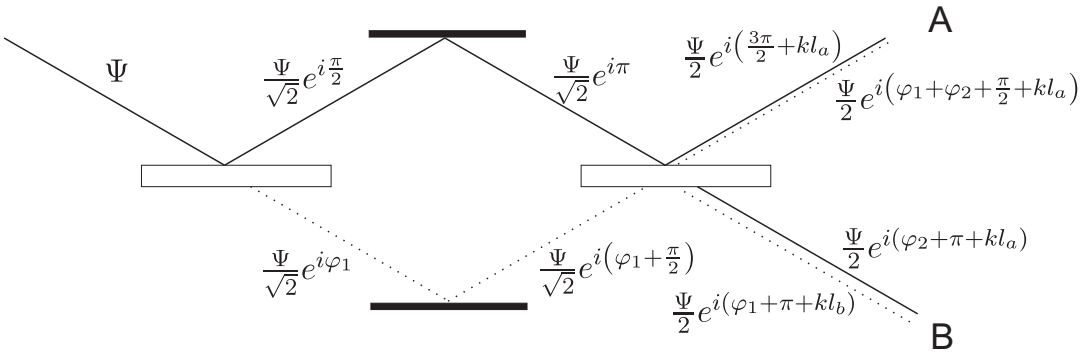


***Figure 2.1:*** *Sketch of a Mach-Zehnder interferometer where the wave functions at the appropriate positions are given. A and B are the detectors where the atoms are counted. We assume that every reflection introduces a phase shift of $\pi/2$ for simplicity. $\varphi_1$ and $\varphi_2$ denote the phase shifts added by passing the beam splitters 1 and 2 respectively.*

$$\langle N_A\rangle = \frac{|\Psi|^2}{2}\left|\left(e^{i\left(\frac{3\pi}{2}+kl_a\right)} + e^{i\left(\varphi_1+\varphi_2+\frac{\pi}{2}+kl_b\right)}\right)\right|^2 \tag{2.1}$$

$$= \frac{|\Psi|^2}{2}\left(2 + e^{i(\pi-\varphi_1-\varphi_2+k(l_a-l_b))} + e^{-i(\pi-\varphi_1-\varphi_2+k(l_a-l_b))}\right) \tag{2.2}$$

$$= \frac{N}{2}\left(2 - 2\cos k(l_a - l_b)\right) \tag{2.3}$$

$$= N\sin^2\frac{\varphi_{ab}}{2} \tag{2.4}$$

Here the relative phase between both arms $\varphi_{\mathrm{ab}} = k(l_a - l_b)$ and the wave vector $k = 2\pi/\lambda$ with $\lambda$ being the wavelength has been introduced and the phases added when transmitting the beam splitters has been set to $\varphi_1 = \pi = \varphi_2$ for simplicity. It was also used that the initial wave function is normalized to the total atom number $N$. Deriving the signal on the second detector yields:

$$\langle N_B\rangle = N\cos^2\frac{\varphi_{\mathrm{ab}}}{2} \tag{2.5}$$

The uncertainty of the phase in terms of the uncertainty of the atom number measurement can be written in the following way.

$$\Delta N = \left|\frac{\partial N}{\partial\varphi}\right|\Delta\varphi \tag{2.6}$$

Calculating the uncertainty of the atom number measurement using $(\Delta N)^2 = \langle N_i^2\rangle - \langle N\rangle^2$ yields (see [22, 23]):

$$\langle\Delta N_i\rangle = \frac{\sqrt{N}}{2}\sin\varphi_{\mathrm{ab}} \tag{2.7}$$

From this the phase uncertainty is derived as

$$\Delta\varphi_{\mathrm{ab}} = \frac{1}{\sqrt{N}} \tag{2.8}$$

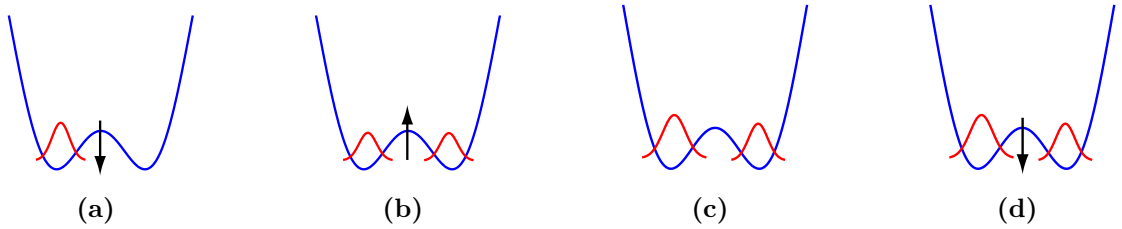


***Figure 2.2:*** *Interferometry with a BEC in a double well potential trap. At first the BEC is prepared in one lattice site. Then the barrier is lowered (a) and raised again (b), which corresponds to a beam splitter. Both split condensates can the evolve in time (c). To convert the phase difference to atom number difference a second beam splitter is applied and the atom number is counted in each lattice site. An experimental sequence for an atom interferometer in a double well potential would be: (a) ⇒ (b) ⇒ (c)⇒ (d) ⇒ (b) ⇒ image*

There are also ways to overcome this limit by using correlated particles at both input ports of the interferometer. In [24] the authors show that one can even reach the Heisenberg limit $1/N$ for the detection of the relative phase by using entangled Bose-Einstein condensates. This limit is also achievable using correlated fermions [25]. For a review article on the precision limits of a quantum interferometer see [21] and references therein.

The above mentioned description is not only valid for an spatial interferometer as depicted in fig. 2.1. In an experiment using Bose-Einstein condensates, the interferometer would be in time. An analog procedure is depicted in fig. 2.2. In the beginning the BEC is located in one well of the double well system, corresponding to one interferometer input (see fig. 2.2a). The first beam splitter is modeled by reducing the barrier and therefore allowing the BEC to populate both wells. In the next step the barrier is raised (see fig. 2.2b) and the condensates in both lattice sites can evolve independently (fig. 2.2c). To overlap both again as in the case of an interferometer for light, the barrier is lowered and the phase difference is transcribed to an atom number difference (fig. 2.2d). The above mentioned detectors A and B are now replaced by the two lattice sites of the trap, where the atom number is counted in each well. An experimental sequence for an atom interferometer in a double well potential would be: (a) ⇒ (b) ⇒ (c)⇒ (d) ⇒ (b) ⇒ image.

This can be described theoretically using the Bose-Hubbard Model. The following description follows derivation given in [26].

## 2.2 Theoretical description of a BEC interference experiment

If the energy splitting between the ground state and the first excited state in the double well potential is small compared to the splitting between the first excited state and all higher states the two-mode model is a good description of the system. In that model, only the two lowest states are treated and all the higher ones are neglected. To describe the interference experiment of a BEC in a double well potential the two-mode Bose-Hubbard

model can be used. In this description the Hamiltonian reads:

$$\mathscr{H} = -\frac{E_J}{N}\left(a^\dagger b + b^\dagger a\right) + \frac{E_c}{4}\left(a^\dagger a^\dagger a a + b^\dagger b^\dagger b b\right) \tag{2.9}$$

where $a$ and $b$ are the annihilation operators for the left/right side of the double well potential. $a^\dagger$ and $b^\dagger$ denote the corresponding creation operators. The first term in this equation corresponds to the particle exchange between both wells, as it describes the annihilation of one particle on one side and the creation of one particle on the other side which corresponds to a tunneling of the particle through the barrier. Hence $E_J$ is denoted as the Josephson tunnelling energy. In this description the number of atoms in the left [right] well can be calculated by $n_l = a^\dagger a$ [$n_r = N - n_l = b^\dagger b$], so the term on the right side of eq. (2.9) is proportional to the atomic density squared and describes the on-site interaction between the particles. The total atom number is given by $N = n_l + n_r$ and $E_c$ is denoted as the charging energy and labels the energy needed to bring one atom from infinity to the trap.

The most general state vector according to eq. (2.9) in the number state basis (Fock basis) is a superposition of all the number states

$$|\Psi\rangle = \sum_{n_l} c_{n_l} |n_l, N - n_l\rangle \tag{2.10}$$

$$\text{where} \quad |n_l, N - n_l\rangle = \frac{\left(a^\dagger\right)^{n_l}}{\sqrt{n_l!}} \cdot \frac{\left(b^\dagger\right)^{N-n_l}}{\sqrt{(N-n_l)!}} |0, 0\rangle \tag{2.11}$$

The coefficient $c_{n_l}$ assigns the initial state of the system. With this ansatz the action of the Hamiltonian (2.9) is

$$\begin{aligned}\mathscr{H} \sum_{n_l} c_{n_l} |n_l, N - n_l\rangle = \sum_{n_l} \Bigg[ &\frac{E_c}{4}\Big(n_l(n_l - 1) + (N - n_l)(N - n_l - 1)\Big) c_{n_l} \\ &- \frac{E_J}{N}\left(\sqrt{(n_l + 1)(N - n_l)}\, c_{n_l+1} + \sqrt{n_l(N - n_l + 1)}\, c_{n_l-1}\right)\Bigg] |n_l, N - n_l\rangle\end{aligned} \tag{2.12}$$

In a Fock state basis this equation can be written in a tridiagonal form with $(N + 1)$ x $(N + 1)$ entries.

In the limit of large atom numbers ($N \gg 1$) the difference between $N$ and $N - 1$ is negligible and the approximation of $N(N - 1) = N^2$ is valid. Introducing the relative atom number difference between the left and the right well

$$n = \frac{1}{2}\left(n_l - n_r\right) \tag{2.13}$$

yields for the atom number in those wells $n_l$ and $n_r$:

$$n_{l/r} = \frac{N}{2} \pm n \tag{2.14}$$

With this expression the term $\sqrt{(n_l + 1)(N - n_l)} \approx \sqrt{n_l(N - n_l)}$ turns into

$$\sqrt{(n_l+1)(N-n_l)} \approx \frac{N}{2}\sqrt{1-\frac{4n^2}{N^2}} \tag{2.15}$$

leading to the action of the Hamiltonian:

$$\mathscr{H}\sum_{n_l} c_{n_l}\,|n_l, N-n_l\rangle = \sum_{n_l}\left[\frac{E_c}{4}\Big(n_l(n_l-1)+(N-n_l)(N-n_l-1)\Big)c_{n_l} - 2E_J\left(c_{n_l+1}\cdot\sqrt{1-\frac{4n^2}{N^2}}+c_{n_l-1}\cdot\sqrt{1-\frac{4n^2}{N^2}}\right)\right]|n_l, N-n_l\rangle \tag{2.16}$$

## 2.3 Phase Revival

In the limit $E_c \gg E_J$ the second term in eq. (2.16) can be neglected. This limit corresponds to the Fock regime where quantum fluctuation are enhanced as will be pointed out later. The action of the Hamiltonian reads:

$$\mathscr{H}\sum_{n_l} c_{n_l}\,|n_l, n_r\rangle = \sum_{n_l,n_r}\frac{E_c}{4}\Big(n_l(n_l-1)+n_r(n_r-1)\Big)c_{n_l}\,|n_l, n_r\rangle \tag{2.17}$$

This equation yields, that in this limit the number states $|n_l, n_r = N-n_l\rangle$ are the eigenstates of the system. The time evolution of every eigenstate is then given by

$$|n_l, n_r\rangle_t = \exp\left[\frac{it}{\hbar}\frac{E_c}{4}\Big(n_l(n_l-1)+n_r(n_r-1)\Big)\right]|n_l, n_r\rangle_{t=0} \tag{2.18}$$

Since every number state $|n_l, n_r = N-n_l\rangle$ is an eigenstate of the Hamiltonian the time evolution is just a phase factor. Every number state picks its own phase, dependent on its population. Given that the initial state is a sum over many number states (see eq. (2.10)) its phase gets completely random - the phase diffuses. By performing an interference experiment with both well sites populated interference fringes can be observed in every realization. As it is shown by J. Dalibard two BEC's, each of them containing a well defined number of atoms will show a perfect fringe visibility as they are released from the trap [27]. This is explained by the "build up" of the phase during the measurement process. An averaging of many realizations indeed yields that the fringes are smeared out, which denotes that the relative phase is random between both wells.

The phase of every number state is $E_c t/4\hbar\cdot(n_l(n_l-1)+n_r(n_r-1))$ and the initial state revives if the phase of every number state is a multiple of $2\pi$. Note that $n_{l/r}(n_{l/r}-1)$ is always an even number, leading to the following expression for the revival time ($m \in \mathbb{N}$):

$$t_m = \frac{4\pi\hbar m}{E_c} \tag{2.19}$$

So when averaging over many experimental realizations at each time step one would first see the interference fringes vanishing. When the evolution time gets close to $t_m$ the fringes would come back, or in other words revive.

In the double well system the external potential can be described by

$$V_{\text{ext}} = \frac{1}{2}m\left(\omega_x^2x^2+\omega_y^2y^2+\omega_z^2z^2\right)+\frac{1}{2}V_0\left[\cos\left(\frac{2\pi}{q_0}x\right)+1\right] \tag{2.20}$$

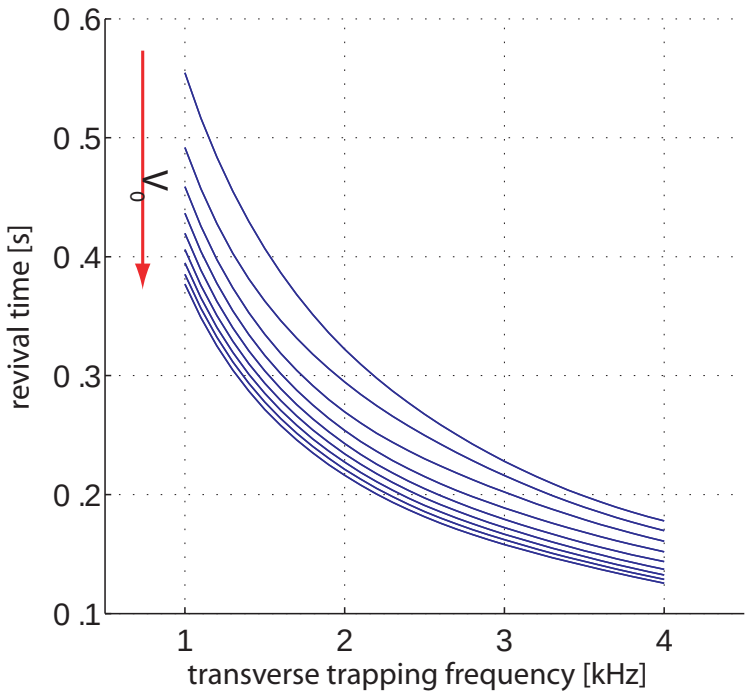


***Figure 2.3:*** *First revival time (m=1) for different barrier heights as a function of the transversal trapping frequency. The different lines account for different barrier heights $V_0$, starting at $V_0 = 4$ kHz in steps of 2 kHz. The parameters used for this calculations have been: 2000 atoms, the longitudinal trapping frequency was kept constant at $2\pi \cdot 250$ Hz, and the lattice spacing was $4.8\,\mu m$*

with $\omega_i$ being the trapping frequencies in direction $i$, $m$ the mass of $^{87}$Rb and $q_0$ the spacing between two maxima of the periodic potential, created by a standing light wave. $V_0$ denotes the barrier height of the double well.

In fig. 2.3 the time of the first revival (m=1) is plotted as a function of the transversal trapping frequency $\omega_\perp$. The different lines denote different barrier heights $V_0$, starting at $V_0 = 4$ kHz and increasing $V_0$ is steps of 2 kHz. The increasing values of the barrier height are plotted in the direction indicated by the red arrow. The revival time is plotted in units of seconds and the trapping frequency in units of $2\pi$.

## Gross-Pitaevskii approach

In order to discuss other regimes of the behavior of the double well system we follow a different approach given in [28]. Since this way of describing a double well potential is already discussed in PhD and Diploma theses of our group [29, 30, 31, 32] and can also be found in several articles [28, 33, 34] only a brief overview is presented here.

To describe a system of many bosons where interactions between the atoms play a role, a *mean field* approach can be used meaning that the interatomic interactions of one particle are described by an average effective potential describing all the other particles at zero temperature. This approach was introduced by E. Gross [35, 36] and L. Pitaevskii [37].

The interaction is described by a point-like interaction with strength $g = 4\pi\hbar^2 a/m$, that only depends on the mass and the s-wave scattering length since it is assumed to be at very low temperatures where all higher angular momentum collision processes are frozen out. The obtained equation is the *Gross-Pitaevskii equation* (GPE) which reads

$$i\hbar\frac{d\Psi(r,t)}{dt} = \left[-\frac{\hbar^2}{2m}\Delta + V_{\text{ext}} + g|\Psi|^2\right]\Psi(r,t) \tag{2.21}$$

In this description the wave function is normalized to the total atom number $N$ as $\int dr|\Psi(r,t)|^2 = N$. The stationary solution can be obtained with the ansatz $\Psi(r,t) = \Psi(r)\exp\left[-i\mu t/\hbar\right]$, where the chemical potential $\mu = \partial E/\partial N$ of the atoms is introduced. With this the GPE reduces to

$$\left(-\frac{\hbar^2}{2m}\Delta + V_{\text{ext}} - \mu + g|\Psi(r)|^2\right)\Psi(r) = 0 \tag{2.22}$$

The chemical potential is fixed by the above mentioned normalization condition to the atom number.

Deriving the energy spectrum of the GPE yields that the spacing between the first excited state and the higher ones is much bigger than the spacing between the ground state and the first exited state[1] (see fig. 2.5). Therefore only the two lowest modes are taken into account. This is done by determining the lowest symmetric $\phi_+$ and antisymmetric $\phi_-$ solutions of the stationary system and then taking the linear combinations of them (see fig. 2.4).

$$\phi_{l,r}(r) = \frac{1}{\sqrt{2}}\big(\phi_+(r) \pm \phi_-(r)\big) \tag{2.23}$$

Note that $\int |\phi_i|^2 \mathrm{d}r = 1$ where $i \in \{+,-,l,r\}$.

[1] and of course the temperature must be sufficiently low

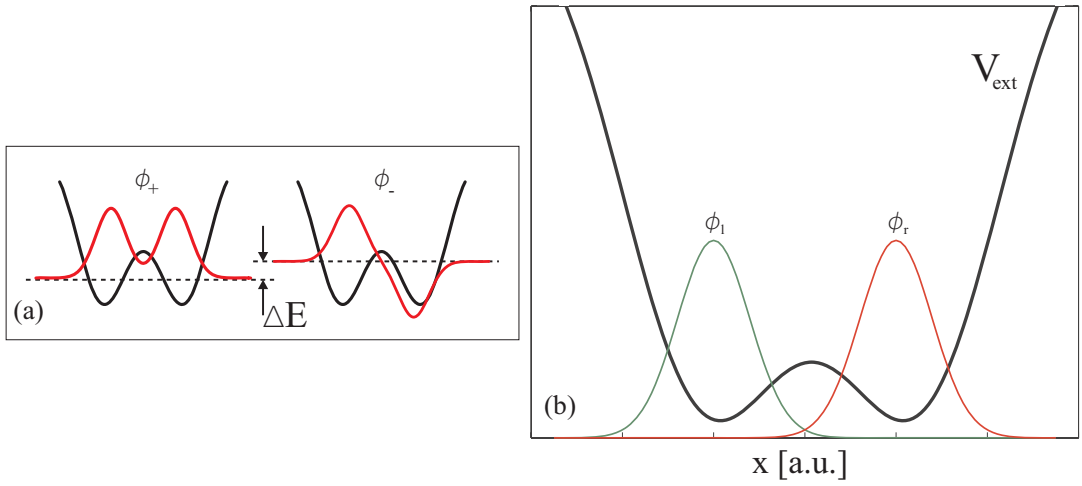


***Figure 2.4:*** *In (a) the ground state and the first excited state of the two mode hamiltonian in the symmetric/antisymmetric basis state is depicted, both separated by an energy gap $\Delta E$. In (b) the two modes are depicted in the left/right basis. In both the black solid line corresponds to the external trapping potential $V_{ext}$*

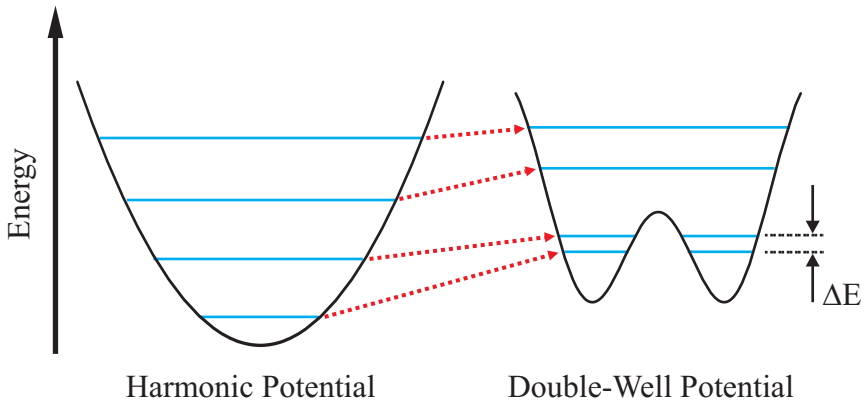


***Figure 2.5:*** *Level spacing between the lowest states in a harmonic potential in comparison to the double well potential.*

Doing this the wave function is assumed to be a superposition of the new left/right states $\phi_{l,r}$ with some complex, time dependent amplitudes[2] $\psi_{l,r} = \sqrt{N_{l,r}(t)}\, e^{i\varphi_{l,r}(t)}$. According to this the wave function reads

$$\Psi(r,t) = \phi_l(r)\sqrt{N_l(t)}\, e^{i\varphi_l(t)} + \phi_r(r)\sqrt{N_r(t)}\, e^{i\varphi_r(t)} \tag{2.24}$$

This ansatz in inserted into the time dependent GPE (2.21) using as new variables the relative phase between both wells and the relative atom number difference (2.13) as defined in the previous discussion concerning the Bose-Hubbard model.

$$\Phi(t) = \varphi_r(t) - \varphi_l(t) \tag{2.25}$$

$$n(t) = \frac{1}{2}\left(N_l(t) - N_r(t)\right) \tag{2.26}$$

With this approach the Hamiltonian for the system reads

$$\mathscr{H}_{TM} = \frac{1}{2}E_c\, n(t)^2 - E_J\sqrt{1 - \frac{4n(t)^2}{N^2}}\cos\Phi(t) \tag{2.27}$$

Wherein $E_J$ is the Josephson coupling energy which gives an estimate for the overlap of the wave functions of the left and right site of the double well and hence describes the tunneling of the particles between both wells. $E_c$ is the on-site interaction energy (or charging energy) and describes the local interaction within both wells.

$$E_c = 8\kappa_{+-} \tag{2.28}$$

$$E_j = \frac{N}{2}(\mu_- - \mu_+) - \frac{N(N+1)}{2}(\kappa_{--} - \kappa_{++}) \tag{2.29}$$

$$\text{where } \kappa_{i,j} = \frac{g}{2}\int |\phi_i|^2|\phi_j|^2 \mathrm{d}r \text{ with } i,j = (+,-) \tag{2.30}$$

These expressions are taken from the paper of T. Bergeman [28].

By expanding now the last term of eq. (2.27) in a series up to the $2^{nd}$ order and neglecting all higher parts, the Hamiltonian gets the form of a harmonic oscillator with the plasma-frequency

$$\omega_p = \frac{1}{\hbar}\sqrt{E_J\left(E_c + \frac{4E_J}{N^2}\right)} \tag{2.31}$$

This is the typical timescale of the dynamics, since tunneling between the wells happens on this scale.

The Gross-Pitaevskii Equation (2.21) describing the double well system has now been simplified in a way that it can be written as a classical pendulum with new coordinates $\Phi$ and $n$. The quantum equation this Hamiltonian is obtained by replacing the variables $n$ and $\Phi$ by their operators such that $[\Phi, n] = i$ (see for example [38] and references therein).

[2]Since $\int |\Psi|^2 \mathrm{d}r = N$ and $\int |\phi_{l,r}|^2 \mathrm{d}r = 1$ the complex amplitudes have to be normalized such that $\int |\psi_{l,r}|^2 \mathrm{d}r = N_{l,r}$ in order to fulfill the condition $N = N_l + N_r$

| **Fock** | **Josephson** | **Rabi** |
|---|---|---|
| $E_c \gg E_J$ | $\frac{E_J}{N^2} \ll E_c \ll E_J$ | $E_c \ll \frac{E_J}{N^2}$ |
| $(\Delta\Phi)^2 \approx \frac{1}{2}\sqrt{\frac{E_c}{E_J}} \gg 1$ | $(\Delta\Phi)^2 \approx \frac{1}{2}\sqrt{\frac{E_c}{E_J}} \ll 1$ | $(\Delta\Phi)^2 \approx \frac{1}{N} \ll 1$ |
| $(\Delta n)^2 \approx \frac{1}{2}\sqrt{\frac{E_J}{E_c}} \ll 1$ | $\frac{(\Delta n)^2}{N} \approx \frac{1}{2}\sqrt{\frac{E_J/N^2}{E_c}} \ll 1$ | $(\Delta n)^2 \approx \frac{1}{4}N \gg 1$ |

***Table 2.1:*** *Phase and atom number uncertainty for three different regimes of $E_c$ and $E_J$ derived from eq. (2.32)*

Deriving the number and phase fluctuations of the ground state leads to the following result

$$\langle \Delta n \rangle^2 = \frac{1}{2}\sqrt{\frac{E_J}{E_c + \frac{4E_J}{N^2}}} \tag{2.32a}$$

$$\langle \Delta \Phi \rangle^2 = \frac{1}{2}\sqrt{\frac{E_c + \frac{4E_J}{N^2}}{E_J}} \tag{2.32b}$$

So the product of the uncertainties in the relative phase and the relative atom number equals one half ($\Delta\Phi\Delta n = 1/2$). From these expressions for the uncertainty of the relative phase and the relative atom number it can be seen that there are three regimes for their behavior. These regimes are denoted by Fock, Josephson and Rabi regime and are shown in table 2.1. In the Rabi regime the phase is very well defined whereas the relative atom number fluctuates $\propto \sqrt{N}$. In the intermediate regime (the Josephson regime) both, the relative phase and the atom number difference are well defined. The opposite case is the Fock regime where the relative phase is completely undefined but the atom number fluctuations are very small. The atoms do not occupy a single macroscopic wave function any more and therefore the mean field approximation is not true any more. This regime was already discussed above using the Bose-Hubbard model, where no mean field approach was done.

## 2.4 Parameters $E_J$ and $E_c$

The previously mentioned Gross-Pitaevskii equation was used to derive the parameters $E_J$ and $E_c$. The calculations have been done, solving the GPE in three dimensions, using a split step Fourier method as described in [29, 32, 39, 40]. The calculations were done using 2000 atoms, a longitudinal trapping frequency of $2\pi \cdot 250$ Hz and a lattice spacing of $4.8\,\mu$m. Due to the cylindrical symmetry of the trap the transversal trapping frequencies are in both directions and have been varied during the calculations.

In fig. 2.6 the necessary barrier heights and trapping frequencies are plotted in order to reach $E_J/E_c = 1$. In fig. 2.6a the ratio $E_J/E_c$ is plotted for different values. The corresponding trap frequencies and barrier heights were found by taking those values corresponding to the minimal values of $(E_J/E_c - 1)^2$. In fig. 2.6b the charging energy $E_c$ is shown as a function of the transversal trapping frequency for different, fixed values

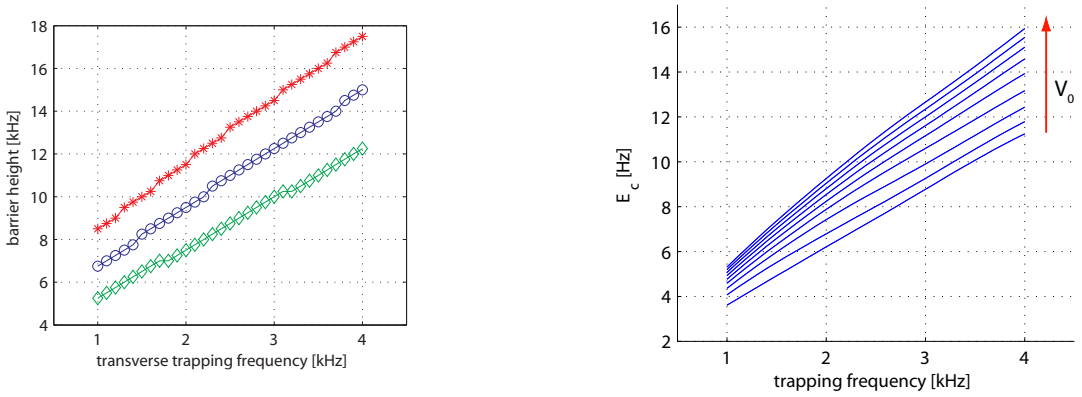


**(a)** **(b)**

***Figure 2.6:*** *Plot of different barrier heights and trapping frequencies to estimate $E_J/E_c$. In (a) the barrier height vs. the transversal trapping frequency is plotted for different ratios of $E_J/E_c$ where the blue circles denote a ratio of 1, the green diamonds a ratio of 100 and the red stars 1/100. In (b) $E_c$ is plotted vs. the trapping frequency for different values of the barrier height $V_0$. $V_0$ increases in the indicated direction by 2 kHz for each line drawn, starting at $V_0 = 4$ kHz. Note that $E_c$ is noted in multiplies of Planck's constant $h$, whereas the trapping frequency is in multiples of $2\pi$. For this calculation we used 2000 atoms, the longitudinal trapping frequency was kept constant at $2\pi \cdot 250$ Hz, and the lattice spacing was $4.8\,\mu$m.*

of the barrier height $V_0$. The barrier height is increased in steps of 2 kHz as indicated by the arrow, starting at 4 kHz. In these calculations the gravitational sag was not taken into account, as it scales as $1/\omega^2$ and is consequently negligible.

# Chapter 3

# How to get a BEC

A great effort has to be taken in order to reach the transition temperature to get a condensate of bosons. Typical transition temperatures are in the range of several nano-Kelvin and therefore 10 orders of magnitude below the room temperature. In comparison to this, the temperature of the cosmic microwave background (CMB) has been measured to be 2.725(2) K, using the COBE satellite (Cosmic Background Explorer) [41]. This is the temperature of the of the space and hence the temperature of the coldest place in nature. And it is still 8 orders of magnitude above the critical temperature for Bose-Einstein condensation. In order to reach that low temperatures, methods of laser cooling and trapping are used, developed in the 1980s. In the following section the main steps necessary to achieve a BEC of $^{87}$Rb atoms will be pointed out. Since this was part of many other works [30, 31, 42, 43, 44] only the most important steps will be presented.

## 3.1 Magneto-Optical Trap

Since the transition temperature to reach the BEC phase is typically in the nK regime one needs to isolate the system as good as possible against any sources that introduce heat to the system. To get rid of collisions with the background gas the whole experiment is done in an ultra-high vacuum chamber (UHV) at a pressure below $10^{-11}$ mbar in a glass cell in order to have good optical access to the system.

$^{87}$Rb dispensers are used as an atom source for the experiments which are placed in a separate part of the chamber, connected to the UHV part by a small hole which acts as a differential pumping stage. In this part we work at a pressure of approximately $10^{-9}$ mbar.

As a first cooling stage a $2D^+$ *magneto-optical trap* (MOT) [45] is used to gather the atoms released by the dispensers. This configuration produces an atomic beam (called funnel) [42, 46] which is captured by a $3D$ MOT [47].

Our laser system that provides the necessary frequencies consists of a *Coherent MBR 110* Titanium-Sapphire (Ti:Sa) ring cavity laser pumped by a *Verdi V10* frequency doubled, diode pumped Nd:$YVO_4$ (neodymium-yttrium-vanadate) laser. The output power of the Ti:Sa is approximately 1.3 W after the optical isolator and it is locked by doppler free absorption spectroscopy to the first $F = 2 \rightarrow F' = 3$ crossover peak.

This beam is split into three parts and each of them is shifted by means of an acousto-optic modulator (AOM) to the right frequency to get the beams for the funnel, the MOT and the imaging beam. The imaging beam is also used to pump the atoms after the MOT

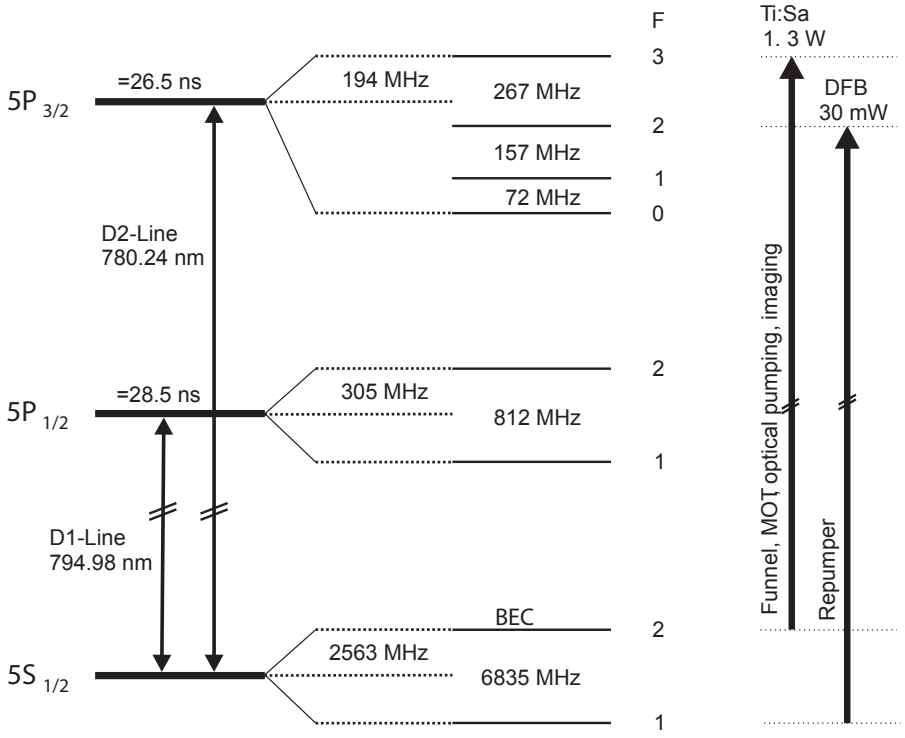


***Figure 3.1:*** *Rubidium-87 line level structure. We use the $F = 2 \rightarrow F' = 3$ transition of the $D_2$ line as cycling transition for cooling. The BEC will occur in the $|F = 2, m_f = 2\rangle$ ground state. The laser frequencies are indicated by the solid arrows*

phase into the low field seeking $|F = 2, m_F = 2\rangle$ state which is used to trap the atoms magnetically.

Since some atoms leave the cycling transition $|F = 2, m_F = 2\rangle \rightarrow |F' = 3, m'_F = 3\rangle$ by falling in the $F = 1$ ground state we need to pump them back. Therefore we use a Distributed Feedback Laser (DFB) by *Toptica Photonics* which provides an output power of 80 mW at maximum.

After trapping the atoms magnetically, optical dipole traps are used for further cooling. Therefore a Nd:YAG (neodymium-doped yttrium aluminium garnet Nd:$Y_3Al_5O_{12}$) laser by *Spectra Physics* with a maximal output power of 7 W is used[1].

For creating the double well potential a second Ti:Sa laser is used. This one is a *Coherent 899-01 Ring Laser* and is pumped by a second *Verdi V10*.

## 3.2 Time-Orbiting Potential Trap

The potential energy for a dipole in a magnetic field reads

$$V(r) = -\mu B(r) = m_F g_F \mu_B |B(r)| \tag{3.1}$$

with $\mu_B$ being Bohr's magneton and $g_F$ the hyperfine Landé factor. Since the Maxwell equations forbid a maximum of the magnetic field in free space only states for which

[1] We run this laser at $\approx 3$ W as otherwise it does not run single mode anymore and we can not get more power through our single mode fibre

the energy is minimized at a field minimum are magnetically trapable. In our case the $|F = 2, m_F = 2\rangle$ state is used.

After the MOT phase the atoms are pumped in that state and are then trapped in a *time orbiting potential* (TOP) trap [48]. The problem of a simple quadrupole trap is its zero field in the center of the trap. As temperature gets lower the probability of the atoms to be at the minimum of the trap increases. At zero field the atoms can undergo spin flips to magnetically not trapped states and leave the trap.

In a TOP trap one overcomes this limitation by adding a rotating bias field. If the frequency of this rotation is much lower than the Larmor frequency of the atoms but much higher than the resulting trapping frequency the atoms see a time averaged potential with a nonzero minimum. The zero is shifted to outside the center and rotates around. The trajectory of the zero field is called "circle of death" because one looses the atoms there. This fact is used to cool the cloud evaporatively by decreasing the radius of the circle of death. The hot atoms which can reach the rim of the trap disappear and therefore the remaining cloud gets colder due to re-thermalization.

With this technique one is able to reach condensation but for studying the dynamics of BEC one has to switch off the trap very fast which is problematic. Hence the cloud is kept uncondensed in the TOP trap and is transferred into an optical dipole trap.

## 3.3 Optical Dipole Traps

For the trapping of atoms in a magnetic field the magnetic moment $\mu$ of the atoms was used. As an electric dipole moment $\vec{d}$ is introduced to the atoms due to the interaction with the external electro-magnetic field they will interact with this light field $\vec{E}$ where the interaction strength is given in the dipole approximation by the Hamiltonian $-\vec{d}\vec{E}$. In the dipole approximation one assumes the electric field (on the order of the wavelength $\lambda$) to be constant over the atom (order Bohr radius $a_0$), which is a good approximation since $\lambda \gg a_0$. Then this potential can be written in terms of the Rabi frequency $\Omega$ and the detuning $\Delta$ of the incident laser beam with respect to the atomic transition $\Delta = \omega_{\text{Laser}} - \omega_{\text{atom}}$ as follows

$$V(r) = \frac{\hbar|\Omega(r)|^2}{4\Delta} \tag{3.2}$$

$$\text{with } |\Omega|^2 = \frac{\Gamma^2 I(r)}{2I_{\text{sat}}} \tag{3.3}$$

$\Gamma$ denotes the natural line width of the transition and the saturation intensity $I_{\text{sat}}$ is given by $I_{\text{sat}} = \frac{\pi c h \Gamma}{3\lambda^3}$. Here we used the *Rotating wave approximation* (RWA) which neglects the terms proportional to $1/\omega_{\text{Laser}}$ comparing to $1/\Delta$ and the detuning was assumed to be much bigger than the natural linewidth ($\delta \gg \Gamma$). For further details on the derivation of equation (3.2) see [49].

If the incident laser beam can be assumed to have a gaussian shape with a waist[2] $\sigma_0$, its intensity as a function of the axial distance from the beam center $r$ and the distance from its waist in longitudinal direction $z$ is

[2] waist here means the minimal transversal distance from the center where the intensity drops to $1/e^2$

$$I(r,z) = I_0 \left(\frac{\sigma_0}{\sigma(z)}\right)^2 \exp\left[-\frac{2r^2}{\sigma(z)^2}\right] \tag{3.4}$$

$$\text{with } \sigma(z) = \sigma_0 \sqrt{1 + \left(\frac{z}{z_R}\right)^2} \tag{3.5}$$

$z_R$ denotes the Rayleigh range $z_R = \frac{\pi\sigma_0^2}{\lambda}$ and gives the distance where the beam radius increases by a factor of $\sqrt{2}$ compared to the waist.

Combining eq. (3.2) and (3.4) arises the trapping potential with the trap depth $V_0 = \frac{\hbar\Gamma^2 P_0}{4\pi\sigma_0^2 I_{\text{sat}}} \frac{2}{3} \left(\frac{1}{2\Delta_{D_1}} + \frac{1}{\Delta_{D_2}}\right)$ (see fig. 3.2a), where the maximal intensity is replaced via $I_0 = \frac{2P_0}{\pi\sigma_0}$ by the beam power $P_0$. The factor $\frac{2}{3}$ considers the Clebsch-Gordon coefficient for the different hyperfine transitions and the factor of 2 is due to the fact that the $D_2$ line is twice as strong as the $D_1$ line. By expanding eq. (3.4) to the $2^{\text{nd}}$ order one can derive the trapping frequencies in radial and longitudinal direction.

$$\omega_\perp = \sqrt{\frac{4|V_0|}{m\sigma_0^2}} \qquad\qquad \omega_\parallel = \sqrt{\frac{2|V_0|}{mz_R^2}} \tag{3.6}$$

Since the trap depth is proportional to the intensity of the beam, evaporative cooling in an optical dipole trap is done by lowering the beam power. Thereby the trap depth is reduced and hot atoms can escape.

The spontaneous emission rate can be considered by calculating the probability to be in the excited state and multiplying this expression by the line width $\Gamma$ which is nothing but the decay rate of the excited state. This approach arises for the spontaneous emission rate $\Gamma_{\text{spon}}$

$$\Gamma_{\text{spon}} = \frac{\Gamma^3 I_0}{8 I_{\text{sat}}} \frac{2}{3} \left(\frac{1}{2\Delta_{D_1}^2} + \frac{1}{\Delta_{D_2}^2}\right) \tag{3.7}$$

Since for our experiments the spontaneous emission rate is below 1 Hz (see fig. 3.2b) its influence can be neglected.

### 3.3.1 Waveguide and Crossed Dipole Trap

The measurements concerning Noise Thermometry [50, 51] have been performed in a $1D$ optical lattice which arises by crossing two focussed laser beams. The *waveguide* beam (WG) makes a confinement in y and z direction with a waist of 60 $\mu$m and the *crossed dipole trap* beam (XDT) a confinement in x direction (see fig. 3.3). The XDT beam was expanded by a cylindrical lens in z direction. The WG had a power of up to 500 mW whereas in the XDT up to 800 mW were used. For the *Noise Thermometry* measurements the trapping frequencies have been $\omega_x = 2\pi\cdot 90(2)$ Hz and $\omega_{y,z} = 2\pi\cdot 100(2)$ Hz respectively. A minimal temperature of $T = 15(4)$ nK could be achieved.

For those measurements it was important to be in the Josephson-regime (see table 2.1) where quantum fluctuations are negligible and the phase fluctuations are of thermal and technical reasons only. To change into the Fock regime one needs to increase the charging energy $E_c$.

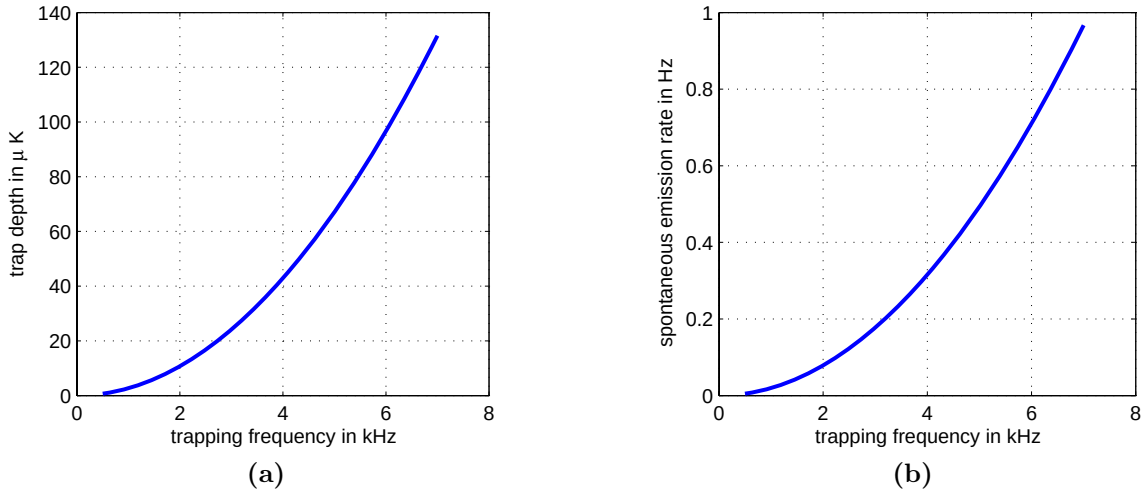


***Figure 3.2:*** *The trapping frequency for the charger in axial direction is used to plot (a) the depth of the dipole trap and (b) the spontaneous emission rate against it.*

### 3.3.2 The new dipole Trap

To obtain this the idea was to increase the trapping frequencies ($\omega \propto \sqrt{P_0}/\sigma_0^2$ to the kHz regime. Since one also needs the spontaneous emission rate ($\Gamma_{\text{spon}} \propto P_0/\sigma_0$) to be rather small, increasing the laser power a lot could not be the solution. Thus a new dipole trap beam with a smaller focus (charger) was installed to increase the charging energy $E_c$. For further details the reader may be referred to chapter 4.

### 3.3.3 Double Well Potential

To create a double well potential we use two gaussian beams, which are large compared to the dipole trap, interfering at the position of the atoms in x-direction. We overlap them and align the resulting interference pattern to the XDT. In the red detuned case an interference maximum in the center[3] of the trap is needed to create a double well potential. This resulting potential can the be described by eq. (2.20) and is shown in fig. 3.3.

## 3.4 Imaging

To image the atoms the destructive absorption imaging technique is used. Therefore $\sigma^+$ polarized light with a gaussian beam shape is shined in which is resonant to the $F = 2 \rightarrow F' = 3$ transition of the $D_2$ line. A constant magnetic field is present in the imaging direction in order to keep the atoms spin-polarized. At a random field only a fraction of atoms would be imaged as the light polarization depends of the quantization axis which is given by the magnetic field.

The imaging system provides a magnification of approximately 10 and uses a commercial objective (*Zeiss Plan-Apochromat S, focal length* $f = 10$ *cm*) to image the atoms

[3] for the interference pattern being blue detuned an intensity minimum in the center is needed since the atoms are then "low field seeking"

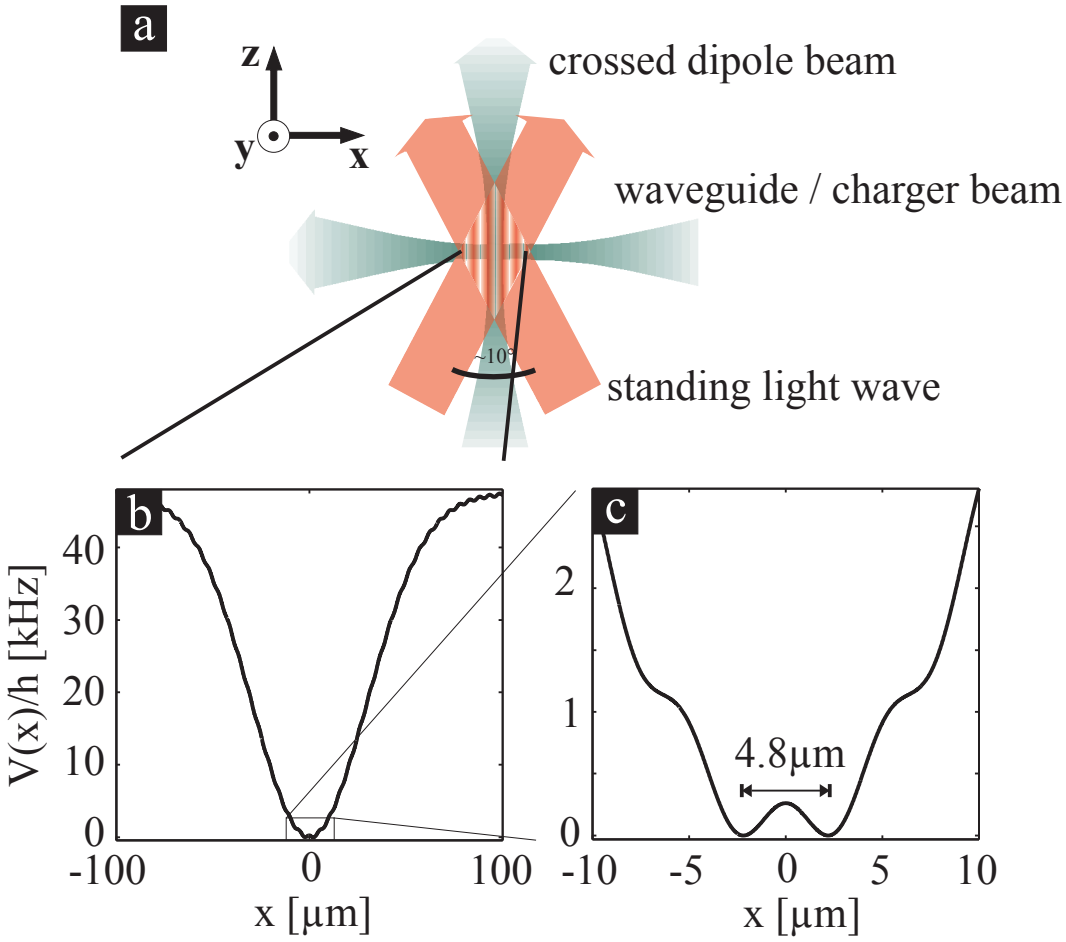


***Figure 3.3:*** *A sketch of the experimental setup to create the double well potential in a trap using either WG and XDT or the Charger is shown in (a). In (b) the resulting potential is shown, where (c) is a cutout depicting the resulting double well potential by adding a harmonic and a cosine potential (see eq. (2.20)), the spacing of the two wells is* $4.8\,\mu m$

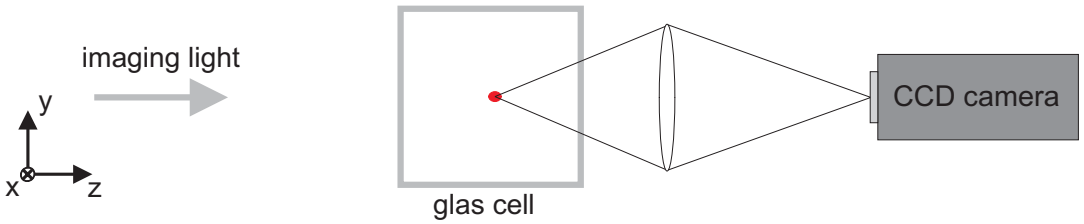


***Figure 3.4:*** *Schematic view on the absorption imaging setup. The atoms (red) are illuminated by a gaussian beam with $\sigma^+$ polarisation and imaged by a 10fold magnification objective onto a CCD chip*

on a CCD-Chip (*Q-Imaging Retiga EXi*) which consists of 1392 x 1040 pixels with a pixel size of 6.45 x 6.45 $\mu$m. The optical resolution of this setup is $r_{\text{Sparrow}} = 2.7\,\mu$m using the Sparrow criterion [31]. The Sparrow criterion corresponds to the distance where the sum of the two Airy-functions of two point sources do not form a clear minimum any longer. This criterion is below the Rayleigh criterion which indicates the distance at which the maximum of one Airy function is at the position of the first minimum of the neighboring Airy function of a point source. For further details on imaging techniques see [42, 52].

As the atoms are heated during the imaging pulse the BEC is destroyed at every picture taken. Hence every picture has to be a new realization of the experiment under the same conditions. Only one picture of the atoms can be taken per shot where all the information has to be extracted. The next picture will be one experimental sequence duration away, which is approximately one minute.

In total we take three pictures per sequence, which is the picture with the atoms $I_{\text{pic}}$, one reference picture $I_{\text{ref}}$ under the same conditions as the atom picture but without atoms.The reference picture is used to remove fringes which occur due to the glass cell or the objective[4].

From these pictures one can derive the relative transfer function $T(x, y)$ where the fringes are removed from the picture and only the atom cloud survives.

$$T(x, y) = \frac{I_{\text{pic}}}{I_{\text{ref}}} \tag{3.8}$$

The transfer function then contains the atom density $\rho(x, y, z)$ integrated along the imaging direction $z$ which is the column density $n(x, y)$. The light propagating through the cloud is absorbed as $\mathrm{d}I = -\rho(x, y, z)\sigma(z)I\mathrm{d}z$ per length element $\mathrm{d}z$ where $\sigma(z)$ is the scattering cross section and should not be mixed up with the radius of a gaussian beam (see eq. (3.5)). The cross section is given by

$$\sigma(z) = \frac{\Gamma}{2} \cdot \frac{h\nu}{I_{\text{sat}}} \cdot \frac{1}{1 + \frac{I(r)}{I_{\text{sat}}} + \left(\frac{2\Delta}{\Gamma}\right)^2} \tag{3.9}$$

Since we image on resonance ($\Delta = 0$) and we are only interested in the column density we can write

[4]The objective we use is not anti-reflection coated

$$-n(x,y) = -\int_{-\infty}^{\infty} \rho(x,y,z)\mathrm{d}z = \frac{2I_{\mathrm{sat}}}{\Gamma h\nu}\int_{I_{\mathrm{in}}}^{I_{\mathrm{out}}} \left[\frac{1}{I} + \frac{1}{I_{\mathrm{sat}}}\right]\mathrm{d}I \tag{3.10}$$

$$n(x,y) = \frac{2I_{\mathrm{sat}}}{\Gamma h\nu}\left[-\log\frac{I_{\mathrm{out}}}{I_{\mathrm{in}}} + \frac{I_{\mathrm{out}}}{I_{\mathrm{sat}}} - \frac{I_{\mathrm{in}}}{I_{\mathrm{sat}}}\right] \tag{3.11}$$

This equation gives the column density for each position $n(x,y)$. Since we are interested in the atom number per pixel we have to consider the pixel size $A$ and the magnification $M$ of the imaging system and we end up with

$$N_{\mathrm{pix}} = \frac{2I_{\mathrm{sat}}}{\Gamma h\nu}\frac{A}{M^2}\left(od + \frac{I_{\mathrm{in}}}{I_{\mathrm{sat}}} - \frac{I_{\mathrm{out}}}{I_{\mathrm{sat}}}\right) \tag{3.12}$$

where we introduced the optical density of the atomic cloud as follows

$$od = -\log\frac{I_{\mathrm{out}}}{I_{\mathrm{in}}} = -\log T(x,y) \tag{3.13}$$

Since it is hard to measure the absolute intensity $I_{\mathrm{out}}$ precisely we skip the term $(I_{\mathrm{in}} - I_{\mathrm{out}})/I_{\mathrm{sat}}$ in the calculation which leads to an overestimation of the atom number of approximately 10%. This overestimation could be decreased by using an intensity, where the atomic transition is not saturated, i.e. $I \ll I_{\mathrm{sat}}$. A more detailed description of our imaging system can be found in [42, 29].

## 3.5 Deducing Temperature

To deduce the temperature of the atomic cloud being trapped in the experiment, the thermal cloud (or the thermal background in case we image a BEC) is fitted with a Maxwell distribution. If the imaging is done *in situ*[5] then the spacial distribution of the cloud can be seen. On the other hand if *time-of-flight* (TOF) images are taken by releasing the cloud suddenly from the confining potential, its momentum distribution is imaged. In the following a short estimation of the expected widths will be given.

The cloud can be described by the following Hamiltonian, letting $\omega_i$ be the trapping frequency in direction $i$ and $m$ the mass of $^{87}$Rb.

$$\mathscr{H} = \frac{p^2}{2m} + \frac{1}{2}m\left(\omega_x^2x^2 + \omega_y^2y^2 + w_z^2z^2\right) \tag{3.14}$$

The phase space density of a thermal cloud is given by the Boltzmann distribution

$$n(r,p) = \mathfrak{z}\exp\left[-\beta\left(\frac{p^2}{2m} + \frac{1}{2}m\left(\omega_x^2x^2 + \omega_y^2y^2 + w_z^2z^2\right)\right)\right] \tag{3.15}$$

The factor $\mathfrak{z}$ in this description denotes the fugacity such that $n(r,p)$ is normalized to the total atom number $N$. If an *in situ* image is taken, an integration over the momenta in the upper equation has to be done, ending up with a density

[5] this is imaging the trap directly

$$n(r) = \int n(r,p)\frac{\mathrm{d}^3p}{(2\pi\hbar)^3} \tag{3.16}$$

$$= \frac{\mathfrak{z}}{\lambda_T^3}\exp\left[-\frac{\beta}{2}m\left(\omega_x^2x^2+\omega_y^2y^2+w_z^2z^2\right)\right] \tag{3.17}$$

The atomic cloud on the taken pictures might be fitted with a gaussian distribution $n(x) = \exp\left[-x^2/2\sigma_i^2\right]/\sqrt{2\pi\sigma_i^2}$. By deducing the width of this fit and comparing it to eq. (3.17) one can estimate the temperature of the cloud as

$$\sigma_i^2 = \frac{k_BT}{m\omega_i^2} \tag{3.18}$$

where $k_B$ denotes Boltzmann's constant.

In a TOF image one looks at the momentum distribution of the cloud and therefor has to integrate over spatial coordinates. The momentum distribution can be rewritten by changing from momentum to velocity $p \to v$. If one expresses the velocity as the distance an atom has moved since the cloud was released, the spacial coordinate is introduced again and can be compared with a gaussian. The observed waist in TOF images is

$$\sigma_i^2 = \frac{k_BT}{m\omega_i^2} + \frac{k_BT}{m}t^2 \tag{3.19}$$

where $t$ denotes the falling time of the cloud. Note that this description is also valid for the condensate fraction in the far field, i.e. the time has to be much larger than the inverse of the trapping frequency ($\omega t \gg 1$). For a deeper insight see for example [53].

# Chapter 4

# The new, strong confining dipole Trap: A way to increase $E_C$

In this chapter the reader will be introduced to the new optical dipole trap (charger), built to increase the charging energy $E_c$ of the double well system. For an insight into the previous setup the reader may be referred to [31, 32, 39]. As already mentioned before, another way of increasing the confinement in the trap would be to increase the power of the laser. This would also increase the spontaneous emission rate and therewith the heating of the atoms in the trap. The third possibility to increase the on-site interaction would be to tune the scattering length via Feshbach resonaces using high magnetic fields.

## 4.1 Optical Setup: beam preparation

Since the Nd:YAG laser cannot be operated at a higher output power than approximately 3 W in order to keep it single-mode,splitting the laser output another time for the third dipole trap was not possible. Single mode fibres are used to clean the mode before going into the experiment to have a gaussian beam profile for the traps. Increasing the laser power further resulted in less output from the fibres indicating a multi mode operation of the laser. The power was needed for the already existing dipole traps of the waveguide (WG) and crossed dipole trap (XDT), which should both be kept.

The new setup is depicted in fig. 4.1. As before the beam coming form the Nd:YAG laser is split by a polarizing beam splitter (PBS) into two. Each of them is passing an acousto-optic modulator (AOM, 80 MHz *Isomet*) to control their intensity before being coupled to a polarisation maintaining single mode fibre made by *Schäfter + Kirchhoff*. These fibres are then guided to the experiment whereas the optics after the fibre was reduced to a minimum in order to conserve the $TEM_{00}$ mode coming out of the fibre as good as possible. The combination of a $\lambda/4$ and a $\lambda/2$ wave plate is used to clean the polarization.

For the charger the zeroth order of the WG arm is used. It is reflected out by a cut mirror, passes a 110 MHz *Crystal Technology* AOM and is then coupled to another polarisation maintaining singlemode fibre.

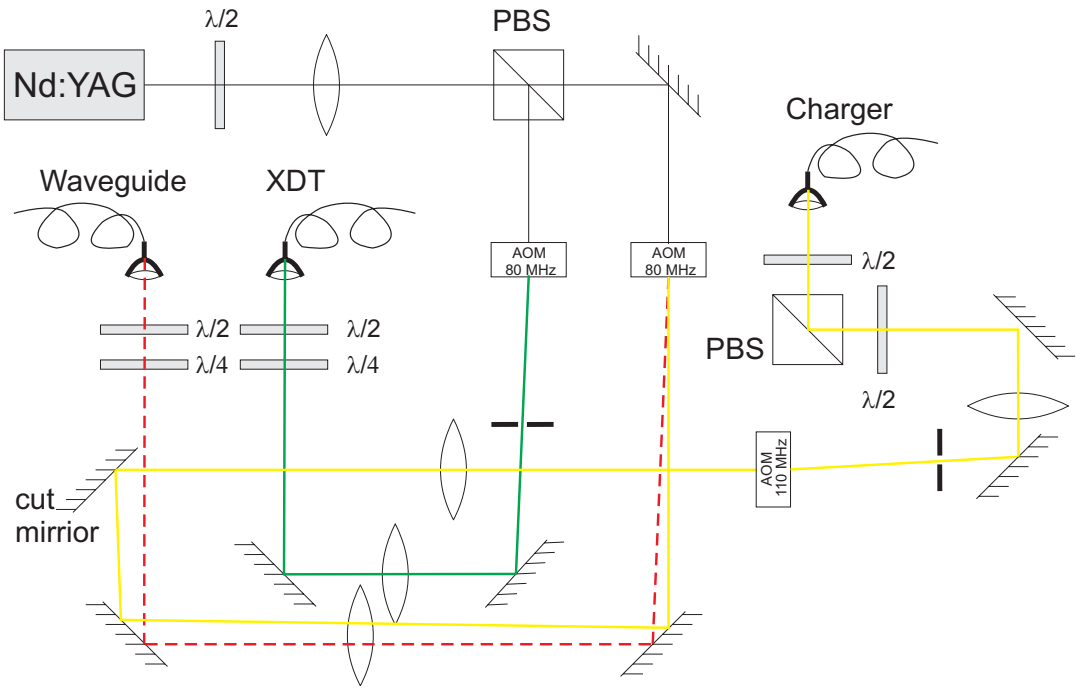


***Figure 4.1:*** *The laser beam is produced by a Nd:YAG Laser and split by a polarizing beam splitter into two, each of them passing an AOM to control the intensity coupled to the fiber. The zero order beam from the waveguide arm is used to produce the charger beam*

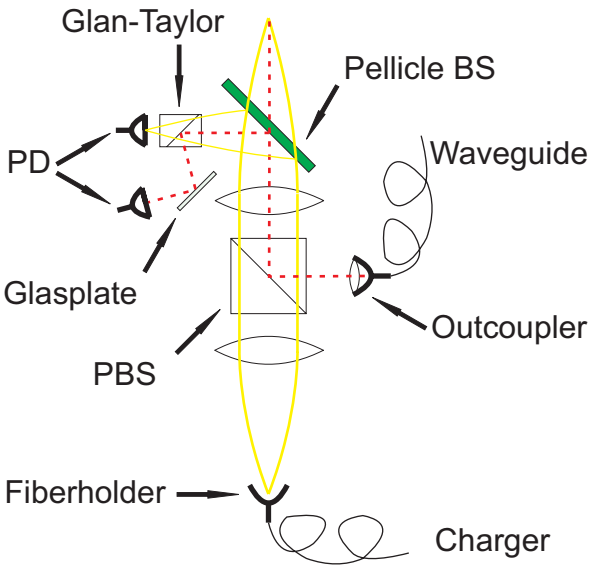


***Figure 4.2:*** *After the Fibre: The yellow beam path depicts the charger and the red one the WG. The charger leaves the fibre divergent, is collimated by an achromatic lens and focused again. The WG is reflected in over a PBS and focused by the same achromat. A pellicle beam splitter is used as a pickup for locking the power of the beams*

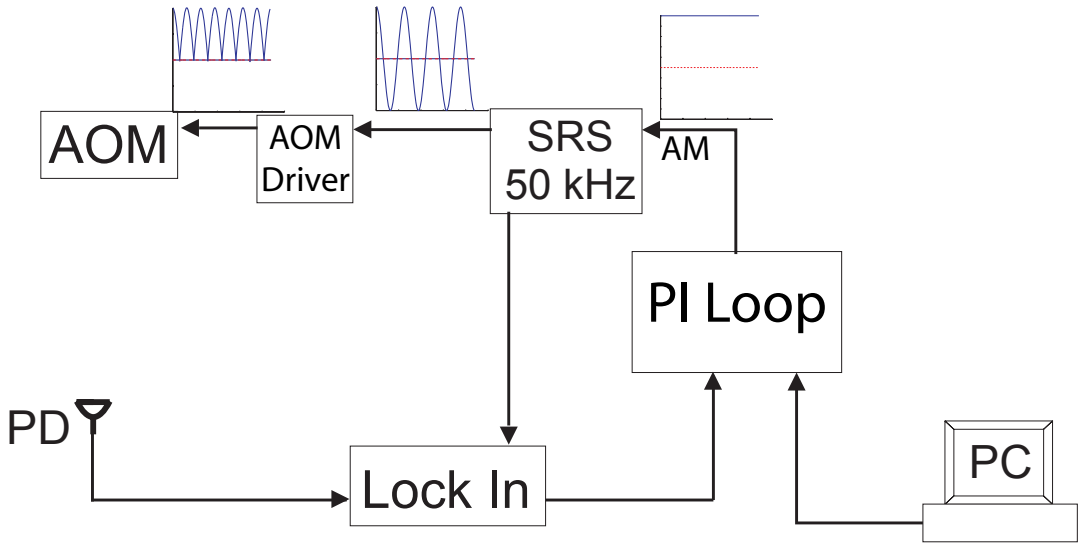


***Figure 4.3:*** *Electronics setup of the intensity lock of the charger. The PI Loop regulates the amplitude of the SRS signal.*

## 4.2 Setup: behind the fibre

The beam setup of the XDT remained unchanged. It leaves the fibre through an outcoupler and is focused by a lens to a waist of 70 $\mu$m.

For the WG and the charger a new massive mount was built, containing both fibres. Both beams are overlapped on a PBS. To fix the charger a fibre holder without any collimation optics is used. The beam leaves the fibre divergent under a half aperture angle of 6.8°. It is collimated by a coated achromatic lens and focused again by an achromat (both lenses: *Melles Griot: 06LAI011/126*).

In order to lock the intensities of both beams, WG and charger, a pellicle beam splitter is used, reflecting 8% of the intensity. Due to their perpendicular polarization, a Glan-Taylor prism divides both beam paths again. The pickup photodiode for the charger is placed in the focal plane, where the WG beam is reflected by another glass plate to further reduce the intensity falling on the photodiode. To distinguish both beams also in the electronics the charger is modulated with 100 kHz whereas the WG is not. We installed a low pass filter onto the WG pickup photodiode to remove the charger signal. Since a high pass filter and a lock-in amplifier is used to read out the charger signal there will also be no information of the WG on it.

The setup used to stabilize the charger intensity is depicted in fig. 4.3. The actual value of interest is set by a computer. We use a feedback loop to control the AOM actively. This gives an output signal, which is modulated by a *Stanford Research Systems DS345* (SRS) arbitrary waveform generator with a frequency of 50 kHz with a peak-to-peak amplitude given by the PI Loop. This modulated signal is sent to the AOM driver which modulates the beam intensity with twice the frequency. After passing the fibre the signal is monitored by a pickup-photodiode as shown in fig. 4.2 and the signal is

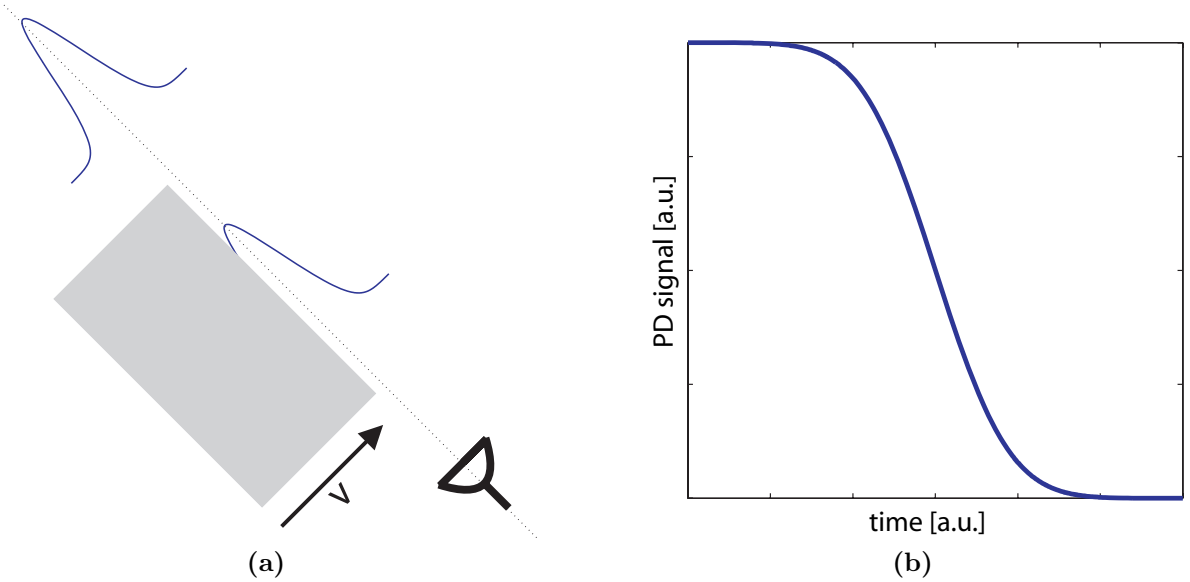


(a) (b)

***Figure 4.4:*** *In fig. (a) the principle of the measurement is depicted. One moves a razor blade (grey shaded area) through the beam and detects the signal on a photodiode. The detected signal vs time (see fig (b)) is then an complementary error function*

detected with a *Femto* Lock-In amplifier which receives the reference signal directly from the SRS and detects the signal in the doubled frequency band. This signal is directed to the loop amplifier which regulates the sum of it and the computer signal to zero.

## 4.3 Spot Size Measurement

To obtain a value for the expected trapping frequencies and trap depths one needs to know the spot size of the trapping beams. Therewith one can also estimate the power needed to create a sufficiently deep trap for loading the atoms from the TOP trap. The first measurement was done by moving a razor blade through the focus. Once the beam was installed and atoms where trapped in it, the spot size was measured with the atoms.

### 4.3.1 Razor Blade method

In the following the beam is assumed to have a gaussian shape. By cutting it at a sharp edge and measuring the total power falling on a photodiode the measured signal corresponds to the complementary error function, which is the integral over a gaussian function $\int_x^\infty e^{-z^2}\mathrm{d}z/\sqrt{\pi}$, as a function of the position where the beam was cut. If the cutting edge is now moved through the beam profile, the complementary error function is directly measured and can be fitted to estimate the beam radius.

Since the waist is defined as the minimal beam radius, only the focus has to be found and the measurement has to be performed there. The data from this measurement is shown in fig. 4.5a for the charger and in fig. 4.5b for the WG. The razor blade has been mounted on a translation stage and was moved with a *Oriel* motor at constant velocity of $200\,\mu\mathrm{m\ s}^{-1}$ through the beam. By moving the whole setup with a second stage in longitudinal direction, the focal point could be found easily.

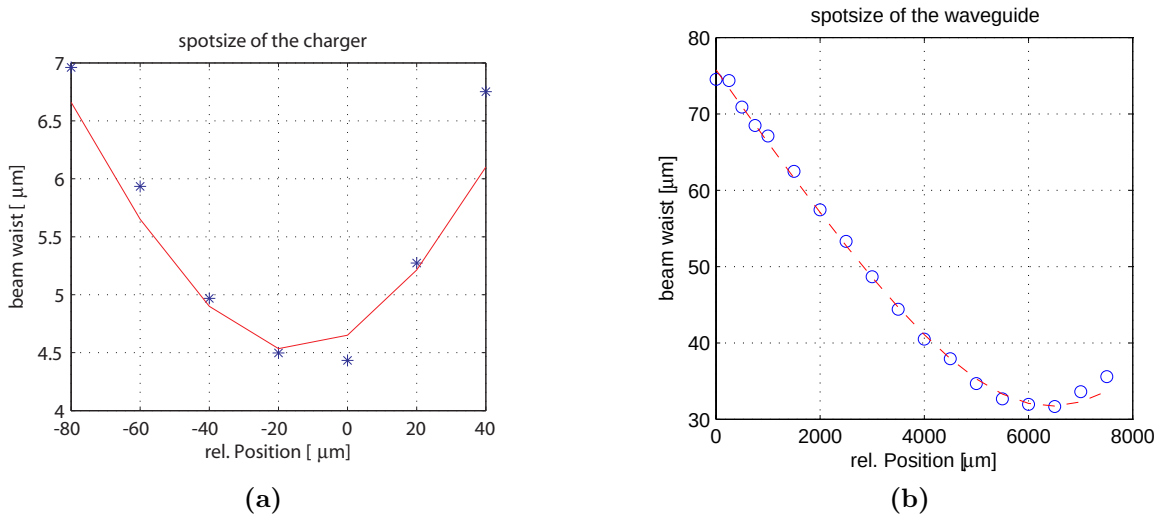


(a) (b)

***Figure 4.5:*** *Measurement of the spot size by moving a razor blade through the beam. In (a) the data for the charger is depicted. The blue stars denote the measured data and the red line the fit to these, giving a waist of* $4.5\,\mu m$*, in (b) the measured data (blue circles) and the fit (red dashed line) for the waveguide is shown giving a waist of* $31.7\,\mu m$*.*

This data was taken using no glass plate between the last lens and the focus. In the experiment the beams have to pass the vacuum cell of course which will influence the wave fronts and slightly blur the focus size. Due to this reason a better estimate for the spot size can be found by using the atoms as a probe.

### Measuring the Trap Frequency

Measuring the trapping frequencies of a trap is quite important as this parameter is needed for all theoretical calculations on the system. Since a detailed description can be found in [29, 43] only the concept is to be presented here.

The idea is to excite a harmonic oscillation in the trap and measure the position of the cloud as a function of trapping time. From the observed oscillation one can deduce the trapping frequency as shown in fig. 4.6a. We use this procedure to calibrate the charger in longitudinal direction as well as to calibrate a trap made by WG and XDT. To calibrate the double well potential a similar sequence is used. One loads a condensate in a harmonic trap, ramps up the barrier quite fast while reducing the harmonic confinement at the same time and such splits the cloud in two, each of them oscillating in the double well potential in one lattice site. By measuring the relative distance between them, the potential height of the barrier can be estimated(for a detailed description see [39]).

Since the optical resolution of the imaging system is $2.7\,\mu m$ [31] oscillations in the transversal direction of the charger are not observable in the harmonic limit. Simple speaking, the trap is too small. Therefore a parametric heating procedure to measure this trapping frequency is used. That is exciting the trap with a certain frequency and measure the width of the cloud (see fig. 4.6b). If the excitation is done with the right frequency heat is introduced to the system, the atoms are excited and the cloud size increases. Right frequency here means modulating with twice the eigenfrequency of the system which is the trapping frequency. This can be understood quite easily since every

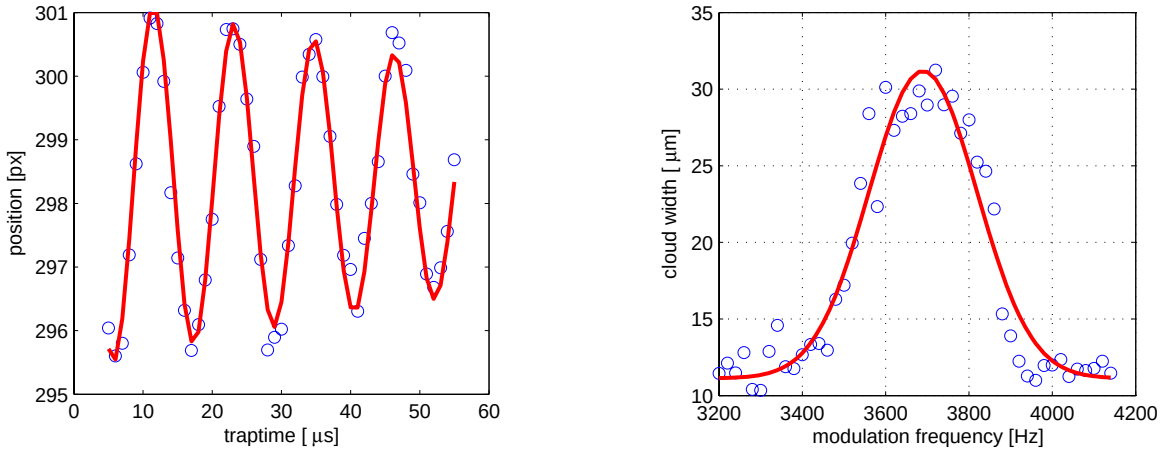


(a) (b)

***Figure 4.6:*** *Measurement of the trapping frequencies of a atom trap with the charger in (a) longitudinal direction by direct observation of an oscillating wave packet yielding $\omega_{\parallel} = 2\pi \cdot 86$ Hz. In transversal direction (b) by means of parametric heating, note that the resonance accords to twice the trap frequency of $\omega_{\perp} = 2\pi \cdot 1850$ Hz. The blue circles denote the measured data points and the red line the fitted curve.*

child does exactly the same when "exciting" a swing. There the oscillation is encouraged by changing the effective length of the pendulum with a frequency which is twice the eigenfrequency. The same is done with the atoms.

### 4.3.2 A direct observation of the trapping geometry using the atoms as a probe

After installing the charger in the setup and loading atoms with it one can also estimate the spot size using trap frequency measurements.

If the trapping frequencies in longitudinal and transversal direction are known, dividing both equations (3.6) leads to the following result and therewith to the spot size of the beam.

$$\frac{\omega_{\perp}}{\omega_{\parallel}} = \frac{\sqrt{2}\pi\sigma_0}{\lambda} \tag{4.1}$$

From this equation and using the measured charger trapping frequencies $\omega_{\parallel} = 2\pi \cdot 86$ Hz and $\omega_{\perp} = 2\pi \cdot 1850$ Hz the spot size can be obtained to be $\sigma_0 = 5.15\,\mu$m. This value is slightly bigger than the measurement using the razor blade. This deviation is an effect of the glass cell, that deforms the wave fronts of the trapping beam and therewith blurs the spot size of the beam.

# Chapter 5

# Three-body loss process in a tight Trap

In the previous chapters a motivation for a tightly confining trap and its properties have been pointed out. The aim for this strong confinement was to increase the on-site interaction in a double well potential, without increasing the spontaneous emission rate of the atoms too much. A high spontaneous emission rate would have increased the heating effects in the trap and would have lead to a rapid loss of the atoms. The loss process due to high atomic densities was studied in the new trap as will be described in the following chapter. The loss procedure could be found to be one and three-body collisions. A theorectical description of these processes yielded that three-body collisions include the possibility to go below shot noise in the precision of the atom number preparation.

In the first part this theoretical description is derived, whereas the second part deals with the measurement of the loss process. For a better understanding of the picture analysis done, a short introduction to CCD-imaging (charged coupled device) and it's noise is pointed out.

## 5.1 Loss Processes in ultracold gases

Many processes lead to heating effects and losses of atoms from the trap. One procedure is the heating due to collisions with the background gas in the cell. In our case this effect is negligible, as the vacuum is good enough to reduce such collisions. The beam intensity of the trapping beams is actively stabilized to remove intensity fluctuations and therewith fluctuations in the trapping potential which also heats the gas. Fluctuations in the pointing of the beams are not corrected, the beams are only mounted on a massive holder and thus we rely on the passive stability of the system. The whole area around the cell is darkened to prevent stray light from heating the atoms.

To model the loss process in a trapped gas of ultracold atoms a rate equation approach is used as it is done in [54]

$$\frac{\partial N(t)}{\partial t} = -K_1 N - K_2 N \langle n \rangle - K_3 N \left\langle n^2 \right\rangle \tag{5.1}$$

In this expression $K_1$ is the one-body loss coefficient taking into account all the loss mechanisms which are independent of the atomic density like power and pointing fluctuations of the trapping beam or the influence of collisions with the background gas,

or the stray light influence. The two-body loss coefficient $K_2$ accounts for the loss due to dipolar relaxation of the atoms from the $(F = 2, m_f = 2)$ state which was magnetically trapped and the losses due to evaporative cooling. This process depends on the mean atomic density $\langle n \rangle$. Three-body collisions are considered by $K_3$. These are events when two atoms form a diatomic molecule and collide with a third one where all the atoms gain the binding energy of the triatomic molecule which is enough to leave the trap. This process depends on $\langle n^2 \rangle$ which reads $\langle n(x,t)^2 \rangle = \frac{1}{N(t)} \int_V n(x,t)^3 d^3x$ and represents the probability of three atoms being close enough that these collisions can occur.

In agreement with [54, 55] we found the two-body loss rate to be negligible compared to the three-body process. As pointed out in [56] this anomaly is due to the coincidence of the scattering lengths for elastic collisions in the $|F = 2, m_F = 2\rangle$ and $|F = 1, m_F = -1\rangle$ states. So for further considerations $K_2$ is assumed to be zero.

### 5.1.1 Loss Process: Master Equation

To model the atom loss of a confined atom cloud by considering one and three body loss processes a master equation is used. The loss process is adopted to be a markovian process, i.e. the history of the system has no influence on the loss rates. If $P(N,t)$ denotes the probability of finding $N$ atoms in the trap at a given time $t$, then its time evolution is given by

$$\frac{\partial}{\partial t} P(N,t) = \sum_{N'} W(N',N)P(N',t) - W(N,N')P(N,t) \tag{5.2}$$

where the rate coefficients $W(N,N')$ were introduced. The gain results from transitions from all other states $N'$ into the considered state $N$ with a rate $W(N',N)$. $W(N,N')$ is the rate of loss from state $N$ into all others with a probability $P(N,t)$.

The probability to lose one atom via one-body-loss is $NK_1$ times the probability to be in state $N$ which is $P(N,t)$. For a three body loss process the probability is $N(N-1)(N-2)K_3$ where the first particle can be chosen out of $N$ particles whereas the next out of $(N-1)$ and so on. So the master equation considering one and three body losses reads

$$\begin{aligned}\frac{\partial}{\partial t} P(N,t) = {} & K_1 \left[(N+1)P(N+1,t) - NP(N,t)\right] \\ & + \frac{K_3}{3} \left[(N+3)(N+2)(N+1)P(N+3,t) - N(N-1)(N-2)P(N,t)\right]\end{aligned} \tag{5.3}$$

Since in literature the three-body loss coefficient $K_3$ is defined in a way that one atom gets lost per collision process, in the above equation a factor of $1/3$ was introduced because here three atoms per event are lost.

In the experiment the mean atom number $\langle N \rangle$ and the variance $(\Delta N)^2 = \langle N^2 \rangle - \langle N \rangle^2$ is measured, so the time evolution of them has to be calculated using the above master equation. Therefore we first calculate the time evolution of the k-th momenta as follows considering here for simplicity only one-body losses.

$$\frac{\partial}{\partial t}\left\langle N^k\right\rangle = \sum_N N^k \frac{\partial}{\partial t} P(N,t) \tag{5.4}$$

$$= \sum_N N^k K_1 \left[(N+1)P(N+1,t) - NP(N,t)\right] \tag{5.5}$$

$$= \sum_N K_1 \left[(N-1)^k N - N^{k+1}\right] P(N,t) \tag{5.6}$$

During the last step the summation index was changed in the first term such that $N \to N+1$. Since the summation then has to start from 1, but a term proportional to $N(N-1)^k$ occurs, a zero is added by starting the summation from zero again.

If three-body losses are included in these calculations the above equations read:

$$\begin{aligned}\frac{\partial}{\partial t}\left\langle N^k\right\rangle = &\sum_N K_1 \left[(N-1)^k N - N^{k+1}\right] P(N,t) \\ &+ \frac{K_3}{3}\sum_N \left[(N-3)^k (N-2)(N-1)N - N^{k+1}(N-1)(N-2)\right] P(N,t)\end{aligned} \tag{5.7}$$

With this equation the time evolution for the mean atom number ($k = 1$) and for the atom number squared ($k = 2$) can be written as follows:

$$\frac{\partial}{\partial t}\left\langle N\right\rangle = -K_1\left\langle N\right\rangle - K_3\left[\left\langle N^3\right\rangle - 3\left\langle N^2\right\rangle + 2\left\langle N\right\rangle\right] \tag{5.8a}$$

$$\begin{aligned}\frac{\partial}{\partial t}\left\langle N^2\right\rangle = &K_1\left[\left\langle N\right\rangle - 2\left\langle N^2\right\rangle\right] \\ &+ K_3\left[6\left\langle N\right\rangle - 13\left\langle N^2\right\rangle + 9\left\langle N^3\right\rangle - 2\left\langle N^4\right\rangle\right]\end{aligned} \tag{5.8b}$$

By introducing the abbreviations for the mean atom number $m = \langle N\rangle$ and for the variance $v = (\Delta N)^2$,the equations for the time evolution of them turn into:

$$\frac{\partial m}{\partial t} = -K_1 m - K_3\left[\left\langle N^3\right\rangle - 3\left\langle N^2\right\rangle + 2m\right] \tag{5.9a}$$

$$\begin{aligned}\frac{\partial v}{\partial t} = &K_1 m - 2K_1 v + K_3\left[-2\left\langle N^4\right\rangle + 9\left\langle N^3\right\rangle + 2m\left\langle N^3\right\rangle\right] \\ &- K_3\left[6m^3 + 9m^2 - 6m + 6mv + 13v\right]\end{aligned} \tag{5.9b}$$

If only one-body losses are treated, $K_3$ is set to zero in eq. (5.9) and the ratio $v/m$ can easily be derived as a function of time.

$$\frac{v}{m}(t) = 1 + \left(\frac{v}{m}\Big|_{t=0} - 1\right)\exp[-K_1 t] \tag{5.10}$$

From this equation it can be seen that the ratio $v/m$ tends to one for long evolution times which means that independently of the initial distribution an atom number will be shot noise limited. This is an effect of the gain term $K_1 m$ in equation (5.9a), which

only arises for discrete atom numbers. If this term is skipped, the ratio $v/m$ tends to zero.

If the three-body loss terms in eq. (5.9) are taken into account, the system is not closed anymore. The equations contain higher momenta which lead to an infinite set of coupled differential equations.

### Gaussian Ansatz

To overcome this problem of an infinite set of differential equations, the initial probability distribution is assumed to have a gaussian shape $P(N, t=0) = \exp\left[-\frac{(N-N_0)^2}{2\sigma^2}/\sqrt{2\pi\sigma^2}\right]$. When solving the master equation numerically it is observed that the distribution can always be approximated by a gaussian. Since the atom number can only be positive, the probability to find zero atoms remains small all the time.

If the probability distribution is supposed to be gaussian at any time the higher moments can be calculated to be

$$\left\langle N^3 \right\rangle = N_0^3 + 3N_0\sigma^2 \tag{5.11}$$
$$\left\langle N^4 \right\rangle = N_0^4 + 6N_0^2\sigma^2 + 3\sigma^4 \tag{5.12}$$

Inserting this in eq. (5.9) yields these coupled differential equations

$$\frac{\partial N_0}{\partial t} = -K_1 N_0 - K_3\left[-N_0^3 - 3N_0\sigma^2 + 3N_0^2 + 3\sigma^2 - 2N_0\right] \tag{5.13a}$$
$$\begin{aligned}\frac{\partial \sigma^2}{\partial t} = {} & K_1 N_0 - 2K_1\sigma^2 + K_3\left[-6\sigma^4 + 3N_0^3 - 9N_0^2 - 6N_0^2\sigma^2\right] \\ & + K_3\left[21N_0\sigma^2 - 13\sigma^2 + 6N_0\right]\end{aligned} \tag{5.13b}$$

A comparison of the time evolution of the master equation and its gaussian approximation is plotted in fig. 5.1 for the mean atom number and the ratio of the variance over mean atom number $v/m$. From these plots it can be seen that the gaussian approximation fits the master equation quite well.

### Going below shot noise

It is also obvious, that the ratio $v/m$ is decreasing below shot noise ($v/m = 1$) which is an effect of the three-body collisions.

This can be observed by looking at the long time limit of three body collisions which is the stationary state for the ratio $v/m$.

$$\frac{\partial}{\partial t}\frac{v}{m} = \frac{1}{m}\frac{\partial v}{\partial t} - \frac{v}{m^2}\frac{\partial m}{\partial t} = 0 \tag{5.14}$$

Keeping in mind that $\sigma \propto \sqrt{m}$ and keeping only the higher order terms one finds for the time derivative of the ratio $v/m$:

$$\frac{\partial}{\partial t}\frac{v}{m} \approx K_3\left(-5mv + 3m^2\right) = 0 \tag{5.15}$$
$$\frac{v}{m} = \frac{3}{5} \tag{5.16}$$

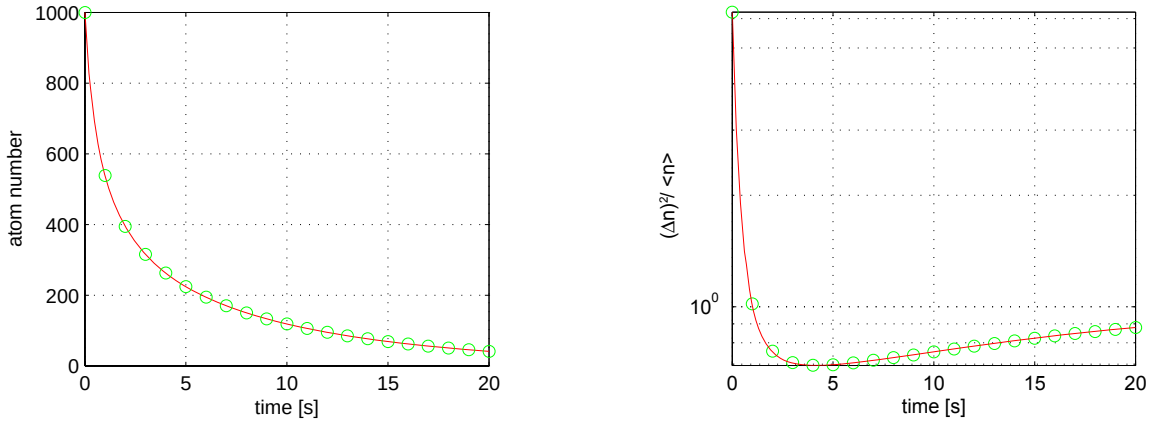


***Figure 5.1:*** *Comparison of the solution of the master equation (green circles) with the gaussian approximation (solid red line) of the cloud density during time propagation. In (a) the evolution of the mean atom number is plotted, in (b) the ratio variance over mean atom number $v/m$ is shown. The parameters for the plot where: $K_1 = 0.1\,s^{-1}$, $K_3 = 1 \cdot 10^{-6}\,s^{-1}$, $N_0 = 1000$ and $\sigma = 2.5 \cdot \sqrt{N_0}$*

If both, one and three-body loss processes are present they will compete and the noise level can go below shot noise. For long time scales, the ratio $v/m$ will level off to one, being shot noise since with decreasing density three-body losses get less pronounced and the loss rate will be dominated by one-body losses. An example for this behavior is plotted in fig. 5.1b where the mean atom number at the beginning is $N_0 = 1000$ with a standard deviation of $2.5 \cdot \sqrt{N_0}$ and one and three-body loss coefficients of $K_1 = 0.1\,s^{-1}$ and $K_3 = 1 \cdot 10^{-6}\,s^{-1}$ respectively.

### 5.1.2 Loss Process: Rolling a Dice

Another way to simulate one and three body losses is a *Monte Carlo* simulation of the process. A dice is rolled for losing the atoms. The probability to lose an atom via one-body loss is $K_1 dt$ where $dt$ denotes the time step one goes further. By starting with a gaussian distribution for the atom number at the beginning and rolling a dice for each atom in every time step for one and three-body loss independently the loss process can be simulated. The three-body loss probability is given via $K_3/3 \cdot N^2 dt$ where three atoms leave the trap. The factor of $1/3$ was introduced to be consistent with the literature, where in case of three-body loss with a rate $K_3$ only one atom is lost.

After each time step the atom number is recalculated and further calculations are done with this new atom number. With this method the time step has to be sufficiently small. If the time step is chosen too large the probability for having a loss process, either one or three-body loss is too big and several atoms get lost in each time step. On the other hand by choosing the time step too small the processing time necessary to calculate the loss increases rapidly. Since several runs have to be averaged, calculating would last an unpractical time. The *MatLab* code for calculating the loss rate with this method is attached in the appendix A on page 51. To improve the calculation time this method was also implemented using *C*. A comparison of both methods also with the gaussian

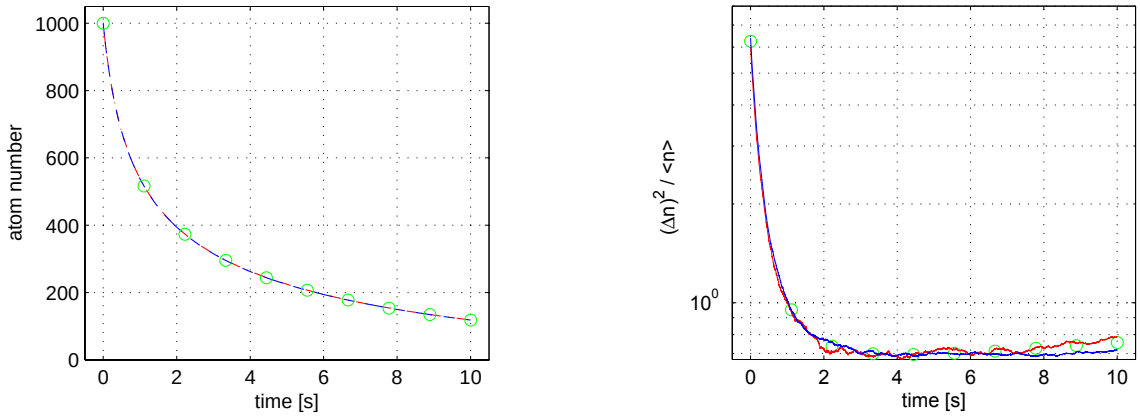


***Figure 5.2:*** *Comparison of the three-body loss using* Monte Carlo *methods implemented in MatLab (red) and using C (blue). The green circles are calculated with the master equation using the gaussian shape approximation. In (a) the mean value is plotted whereas (b) shows the variance over the mean value. The following values were taken:* $K_1 = 0.1\,s^{-1}$, $K_3 = 1 \cdot 10^{-6}\,s^{-1}$ *and* $N_0 = 1000$ *atoms with an initial waist of* $2.5 \cdot \sqrt{N_0}$ *using MatLab* 1500 *runs were calculated, using C* 3000 *runs.*

approximation of the master equation is plotted in fig. 5.2. It can be seen that both methods overlap quite well. The slight difference is an artefact of the limited number of runs which were made to calculate both curves.

For our calculations the time step $dt$ was chosen to be a factor of $10^3$ smaller than the minimal loss rate at the beginning of the process. Hence the probability to lose atoms is very small. The initial atom number follows a Poissonian distribution with a selectable width. The initial atom number as well as the loss coefficients and the initial noise level were taken from the measurements.

In order to proof the influence of the initial noise level 2000 runs were calculated, varying the initial noise. These calculations revealed no big influence of the initial noise level on the possibility to go below the shot noise level. The advantage of the Monte Carlo method to simulate the loss process is, that there is no gaussian ansatz necessary to solve the problem. The good agreement of both methods yields the correctness of the gaussian ansatz to solve the master equation.

## 5.2 CCD Imaging and its Noise

Since all the information of the system is extracted from the images the technical noise of them has to be known quite well and should be reduced as far as possible. In this section the reader will be introduced to the main causes of technical noise and ways to reduce them. As two pictures are taken - the atom picture and the reference picture with everything but the atoms - one has to be sure that the imaging system doesn't move more than a reduced pixel size[1] during the exposure of the pictures. This is achieved by

[1] The reduced pixel size is given by $A/M^2$, where $A$ is the area of one pixel and $M$ is the magnification of the imaging system

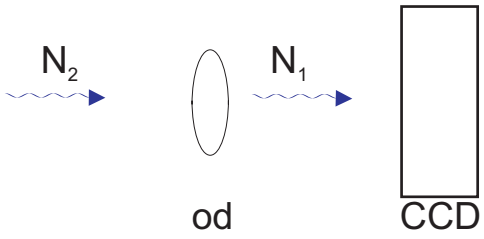


***Figure 5.3:*** *Measuring the optical density (od) of a cloud with a CCD by absorption imaging. Without a cloud $N_2$ photons would reach the detector. With the cloud the number of photons on the detector is $N_1$*

a massive mount for the imaging system.

### 5.2.1 Quantum Efficiency

For detecting the signal of the imaging beam a CCD camera by *QImaging* is used. In a CCD many photosensitive areas of a depleted semiconductor are arranged in an array which is read out by an electronic device, step-by-step by shifting the charges to the side of the chip where the detection of the photoelectrons takes place. The detection of the photons relies on a good photon-to-electron conversion rate, known as quantum efficiency. An ideal quantum efficiency of 1 (100%) would state that every photon excites an electron in the conducting band which is then detected. Achievable values are in the range of 40% for good CCD's and up to 95% for *electron multiplier CCD's* (EMCCD's)[2]. The bigger the quantum efficiency, the smaller the exposure time necessary at a given photon flux to get the same signal. The quantum efficiency of our camera is $\approx 30\%$.

### 5.2.2 Photon Number fluctuations

The fluctuations of the number of photons incident on the CCD during the exposure time can not be influenced by the camera design. Since the number of photons follows a Poissonian distribution the number of photons can only be counted with an error of the square route of the incident number of photons $N$.

$$\Delta N_{\text{photon}} = \sqrt{N} \tag{5.17}$$

If a configuration is assumed as sketched in fig 5.3 with $N_1$ being the number of photons incident on a CCD chip after passing an atom cloud with optical density *od* the number of counted photons would be $N_1 \pm \sqrt{N_1}$. If the illuminated object is removed, $N_2 \pm \sqrt{N_2}$ photons would be counted. So the optical density *od* which is our signal $s$ can be estimated to be:

$$s = \log \frac{N_2}{N_1} = od \tag{5.18}$$

If the noise of the counted photon number is taken into account, the signal reads:

[2] see for example the websites www.qimaging.com or www.hamamatsu.com or www.roperscientific.com

$$s = \log \frac{N_2 + \Delta N_2}{N_1 + \Delta N_1} \approx od + \underbrace{\frac{\Delta N_2}{N_2} - \frac{\Delta N_1}{N_1}}_{\Delta s} \tag{5.19}$$

In this step the log was expanded, assuming $\Delta N \ll N$. The root-mean-square deviation is calculated to be:

$$\left\langle \Delta s^2 \right\rangle = \frac{\Delta N_2^2}{N_2^2} + \frac{\Delta N_1^2}{N_1^2} = \frac{1}{N_2} + \frac{1}{N_1} \tag{5.20}$$

In this calculation the noise of $N_2$ and $N_1$ is assumed to be uncorrelated. Thus the mean of the product of both vanishes.

If all noise sources which are related to the camera could be neglected, the noise level would still be on the order of eq. (5.20) on the picture.

### 5.2.3 Dark Current

Another source of noise is the thermally induced dark counting rate. In a CCD an incoming photon is counted whenever it excites a valence electron over the gap into the conduction band. This electron can then be counted by the read out electronics. But a valence electron can also be thermally excited into the conduction band. This wrongly excited electron will be counted as if it came from a photon signal since it can not be distinguished anymore. This wrongly counted electrons are termed as dark current.

This effect is strongly dependent on temperature. By cooling the CCD the dark current can be reduced to a negligible level.

One can correct the pictures by taking pictures without opening the camera shutter. These pictures have to be of the same exposure time as those which are to be corrected. One can then simply subtract a mean dark image from the pictures. In our setup the dark current is negligible.

### 5.2.4 “Hot” Pixels

Since not all the pixels on a CCD chip have the same sensitivity a homogeneously illuminated surface will not cause the same amount of excited electrons in each pixel. To estimate this effect on the noise a flat field image is taken. This is done by imaging a homogeneously lighted surface and searching for *hot* pixels which have a much bigger counting rate than a mean pixel. Also dark spots like dust can be found in that way.

Such effects can be corrected by dividing the picture by the flat field image after correcting it for the dark current. For our CCD the flat field showed no hot pixels thus we skipped the flat field correction in the images.

### 5.2.5 Read Out Noise

Also the electronics used to read the CCD introduces some noise. The pixels of the CCD chip are read out and the signal is multiplied by a constant gain factor which can be set by the software. After that a constant offset is added to the signal in order to prevent negative counting rates and the up to here analog signal is converted into a digital one. Note that every amplifier adds noise to the signal. If this noise is assumed

to be uncorrelated, its influence can be decreased to a negligible value by taking many pictures. *QImaging* specifies the total read noise of our camera to be $8\,e^-$ per pixel where the pixel saturates at $22 \cdot 10^3\,e^-$ at a binnig of 2 x 2. From this it can be seen that this camera is not limited by the read noise.

### 5.2.6 Binning

One way to enhance the signal-to-noise-ratio (SNR) is to bin some pixels before reading out the signal. By binning the pixels in that way several pixels are treated as one with an increased effective pixel size. Therefore the signal is enhanced for a given exposure time whereas the read noise is the same as for a single, unbinned pixel.

## 5.3 Loss Process: Measurements

A three-body loss measurement was performed by loading approximately $7 \cdot 10^4$ atoms in an optical trap formed by the charger. The trapping frequencies were $\omega_\parallel = 2\pi \cdot 166$ Hz and $\omega_\perp = 2\pi \cdot 3.58$ kHz. Since the trapping frequency in the direction of gravity is that high, the gravitational sag is negligible as it scales with $\omega^{-2}$.

As the trap is formed by a single beam holding the atoms in all three directions, the trapping frequencies in longitudinal and transversal direction are no longer independent of each other. Both are linked by the geometry of the trap via

$$\omega_\perp = \frac{\sqrt{2}\pi\sigma_0}{\lambda}\omega_\parallel \tag{5.21}$$

where $\sigma_0$ stands for the waist and $\lambda$ for the wavelength of the trapping beam, which are both known.

After cooling in the magnetic trap, the atoms are loaded into the charger at the above mentioned trapping frequencies. After holding them in the trap for a variable time the atomic cloud is released and a TOF image is taken after a falling time of 1.15 ms with a binning of 4 times 4 of the CCD camera. The imaging pulse had a length of $400\,\mu$s and its intensity was $I = 0.1 \cdot I_{\mathrm{sat}}$.

To analyze the pictures and deduce the atom number from them several steps are done which will be explained in the following.

Directly after being imaged, a gaussian fit of the pictures is applied where the center position of the cloud and the gaussian width is deduced. Also a cut of the pictures is done where only a 160 x 160 pixel wide area around the position of the atoms is saved. In the final evaluation process the mean center position and the mean width are computed. This is a good measure of the clouds position since the position varies less than 0.2 binned pixel size.

Bad pictures where the atom number is too poor or not yet stable occur mainly at the beginning of the measurement procedure. So the first 500 shots have been removed. In the later measurements the atom number showed no global drifts.

In the next step that part of the picture is selected where the atoms are by taking an ellipse of the form

$$\frac{(x-c_x)^2}{(R\sigma_x)^2} + \frac{(x-c_y)^2}{(R\sigma_y)^2} < 1 \tag{5.22}$$

where $c_x$ and $c_y$ denote the mean center position of the cloud in $x$ and $y$ direction respectively and $\sigma_x$ and $\sigma_y$ the related widths. $R$ is chosen such that 0.1% of a gaussian distribution would be outside the cut which means for a final atom number of 3000 atoms that 3 of them are cut whereas shot noise would be 55 atoms. Hence the error of the cut is far below the noise level.

In the next step the noise of the pictures outside the cut region where no atomic cloud is is analyzed. A box is taken out in every direction, a summation is performed over the "short side" (shown in the 2D plots of fig. 5.4) and a fit with a linear function is applied. If the slope of this fit exceeds a critical value the picture is rejected. An example of such cuts and the noise pictures are shown in fig 5.4.

After that the reference picture is normalized to the background of the atom picture in the region outside the elliptical cut. This normalization factor is always close to one. By doing so small fluctuations in the imaging beam between both pictures are removed. The final picture is achieved with the normalized reference picture, where the atom number is deduced simply by summing over the area within the cut. The noise is then the standard deviation of all the pictures taken.

In order to remove the photon noise eq. (5.20) is used where the sum is taken over the area inside the elliptical cut in the normalized reference picture and in the atom picture to estimate the number of photons before and after passing the atomic cloud. This photon noise is removed from the estimated noise of the pictures by weighting it with the quantum efficiency of the camera of approximately 30%. The comparison between the noise level before and after removing the photon noise is shown in fig. 5.5 where the variance over the mean atom number is plotted with blue stars representing the noise level before removing the photon noise and the red diamonds after it. It can be seen that both curves are inside the errorbars of each other, where one point corresponds to the average of approximately 90 measurements.

After doing this procedure for all the taken pictures we can have a look at the cloud size as a function of the holding time of the atoms in the trap. This plot is shown in fig 5.6a. As it can be seen from this the size decreases with the trapping time which indicates that the cloud cools down due to the loss process [57]. This is the same effect that leads to a cooling due to evaporation. With the help of eq. (3.19) the temperature of the cloud during the loss process can be derived as plotted in fig. 5.6b

If this temperature change should be considered in the loss theory we have to look at the loss on an atomic scale. Let us denote the local three-body loss constant as $k_3$. Since the measurements are in a thermal gas the cloud's density can be approximated to have a gaussian shape. With this approach the local loss coefficient can be integrated over the cloud to estimate the mean loss coefficient $K_3$ as follows

$$K_3 = \int k_3 n(r)^3 \mathrm{d}^3 r = \int k_3 \left( \frac{N}{(2\pi)^{3/2}\sigma_x\sigma_y\sigma_z} \right)^3 \exp\left[ -\frac{3x^2}{2\sigma_x^2} - \frac{3y^2}{2\sigma_y^2} - \frac{3z^2}{2\sigma_z^2} \right] \tag{5.23}$$

$$= k_3 \frac{N^3}{(2\pi\sqrt{3})^3(\sigma_x\sigma_y\sigma_z)^2} \tag{5.24}$$

$$= k_3 \frac{m^3\bar{\omega}^2}{(2\pi\sqrt{3}k_B)^3} \frac{N^3}{T^3} \tag{5.25}$$

In the last step it was used that the width of a thermal gaussian cloud is given by

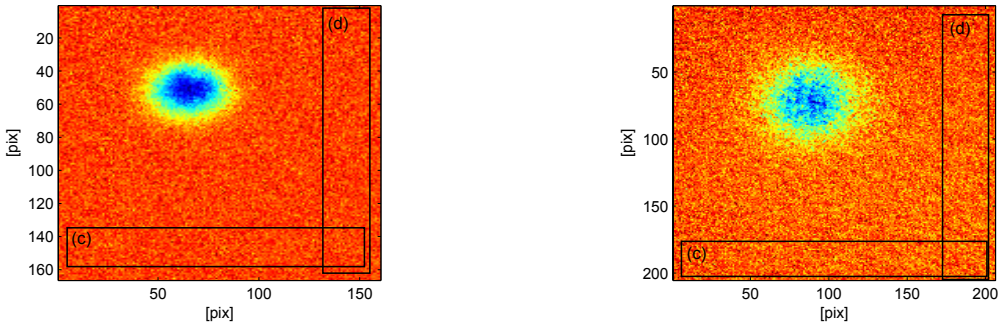


(a)

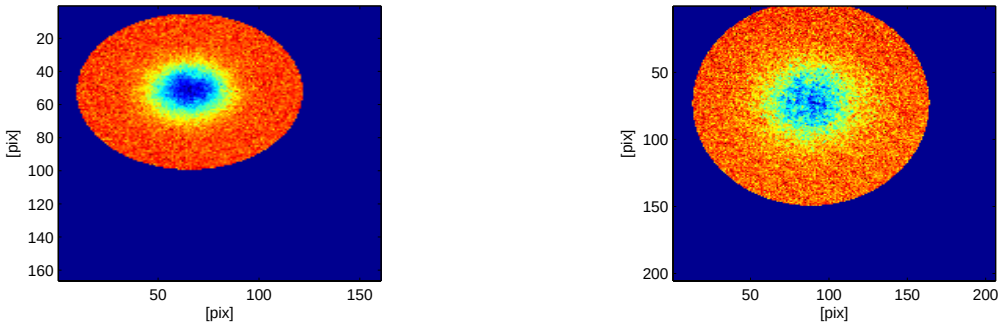


(b)


(c)


(d)

***Figure 5.4:*** *Examples for a good (left) and a bad picture (right). In (a) the picture of the atomic cloud is shown. In (b) a cut was done around the cloud. The inner part will be summed up after normalizing the reference picture to deduce the atom number. (c) and (d) show rectangular cuts of the outer region of (b) where the noise is analyzed. The pictures are summed up over the short side (2D plots) and fitted with a straight line. The pictures on the left hand side show a uniform noise, whereas on the right hand side a clear structure is visible in the noise - such pictures are removed during the analysis. Note that both pictures are not part of the same measuring cycle, therefore the cuts shown in (b) differ.*

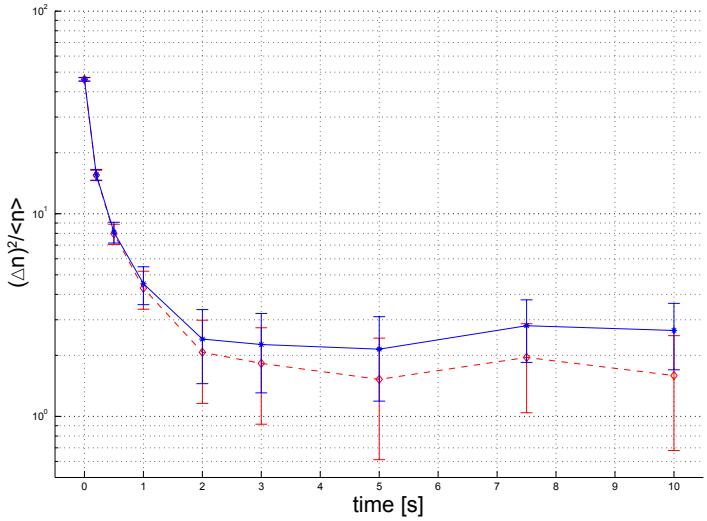


***Figure 5.5:*** *Comparison of the noise level before and after the removal of the photon noise. Plotted is the variance over the mean atom number as a function of the holding time in the trap. The blue stars show the data before and the red diamonds the data after the removal. Each point is measured approximately 90 times.*

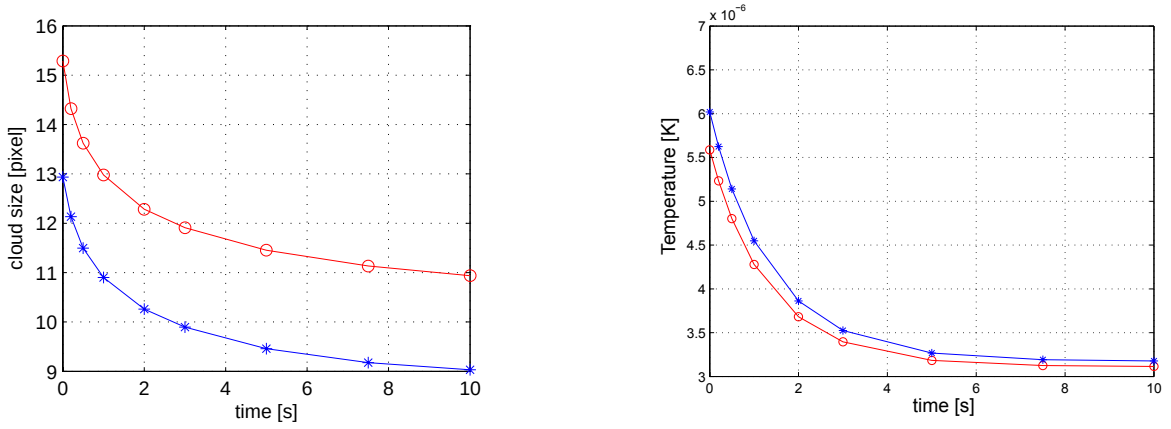


**(a)** **(b)**

***Figure 5.6:*** *In (a) the size of the atomic cloud after TOF is shown as a function of time in the trap. The $x$ direction is denoted by the red circles whereas the blue stars mark the size in $y$ direction. In (b) the deduced temperatures are shown.*

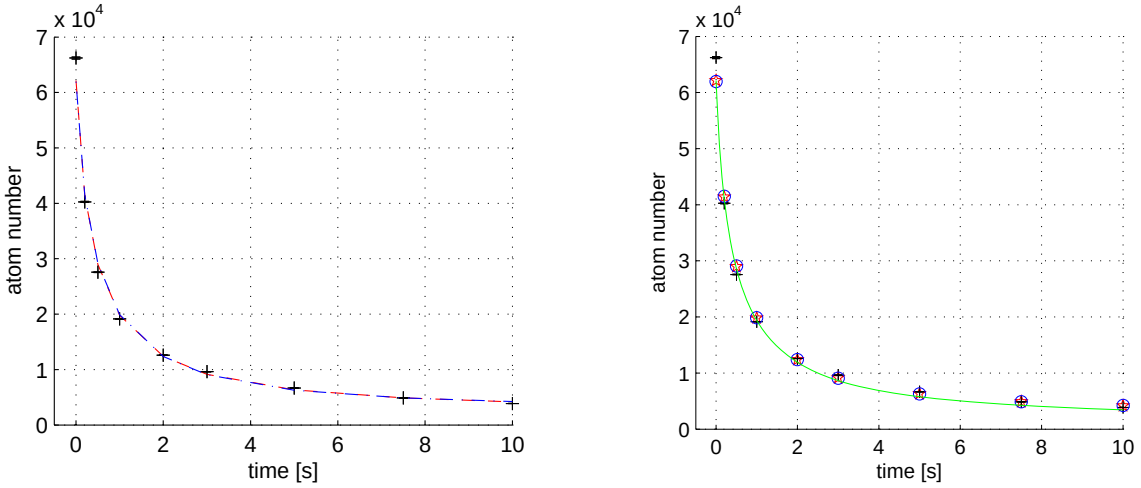


***Figure 5.7:*** *Mean atom number vs holding time in the trap, the black crosses denote the measured data, in (a) the red and blue curves correspond to the fitted curves using the deduced temperature data from $x$ and $y$ direction respectively as is plotted in fig. 5.6b. Both fit the measured data quite well giving an initial atom number of $N_0 = 62000$, $K_1 = 0.025\,s^{-1}$ and $K_3 = 7.46 \cdot 10^{-10}\,s^{-1}$. In (b) these data is reduced to red stars and blue circles respectively and the loss is simulated by the master equation ansatz using the gaussian approximation of the cloud's shape. This data is shown as a green line*

the Boltzmann distribution as eq. (3.18) $\sigma_i^2 = k_B T/m\omega_i^2$ and additionally the geometric mean trapping frequency was introduced as $\bar{\omega}^3 = \omega_x\omega_y\omega_z$.

Now the term $K_3 N \langle n^2 \rangle$ in eq. (5.1) can be replaced by (5.25) and the temperature dependent rate equation for one and three-body loss processes occurs.

$$\frac{\partial N}{\partial t} = -K_1 N - K_3 \frac{N^3}{T^3} \tag{5.26}$$

This equation together with the deduced temperature information of the cloud is used to fit the measured loss data as can be seen in fig 5.7a.

In fig. 5.7b those fitted curves have been reduced to the red stars and blue circles for $x$ and $y$ direction respectively and the simulation is inserted in the figure which fits quite well. The fit results for the loss coefficients were $K_1 = 0.025\,\mathrm{s}^{-1}$ and $K_3 = 7.46 \cdot 10^{-10}\,\mathrm{s}^{-1}$. Those values and the measured initial noise level have been used for the simulation of the loss process using the master equation with the approximation that the shape of the cloud has always a gaussian profile.

If we now have a look at the noise of the pictures it can be observed (see fig. 5.8) that at the beginning of the holding time of the atoms in the trap the noise decreases rapidly. This process is due to the high three-body loss probability at that time. With increasing holding times the three-body losses get less pronounced and at high trapping times the loss is only dominated by the one-body loss mechanism.

In comparison to the expected theoretical curve, the noise level is higher which indicates that we are limited by the imaging system. The general behavior of noise reduction due to the loss process can be observed, but the measurements are still a factor of two above shot noise and a factor of three above the predicted value. This deviation from the

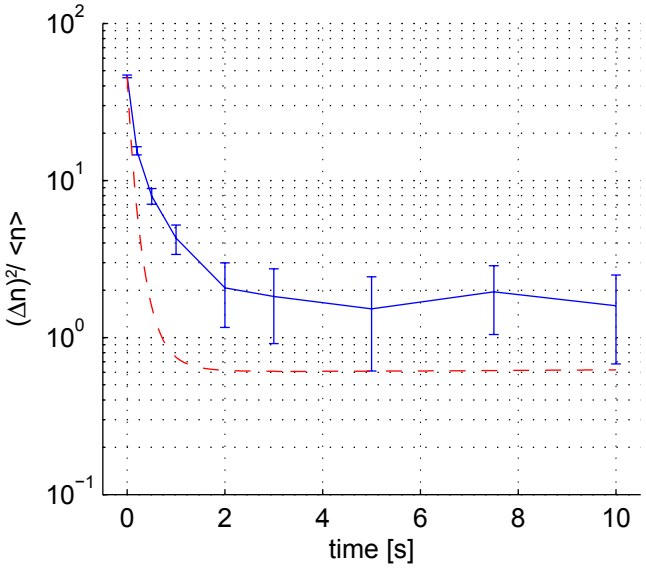


***Figure 5.8:*** *Noise plot of the measured data (solid blue line) and the expected curve (dashed red line) using the fitted values of $K_1$, $K_3$, $N_0$ and level of initial noise. Plotted is the variance over the mean value of time in the trap. The errorbars mark the value of $1/\sqrt{n}$ of the actual value at that point where $n$ is the number of data points taken for the considered trapping time which is at average 90 measurements*

predicted curve indicates a problem of the imaging setup used. A non-coated objective was used that absorbs the beam. This damping leads to a shot noise limitation of the photon number, since it is a linear process (see for example the behavior of the noise level when only one-body losses are present). The same explanation is valid for our glass cell. This is also not coated and hence absorbs the beam. The theoretical curve was calculated using the gaussian approximation of the master equation. Since the mean atom number is in good agreement with the theory the origin of the deviation of the measured to the predicted curve is most likely due to technical reasons. The imaging duration of $400\,\mu$s and its intensity of $I = 0.1 \cdot I_{\text{sat}}$ indicate a movement of the atoms during the imaging pulse of 0.8 mm. This is much more than the rayleigh range of of imaging setup of about $40\,\mu$m. The changing velocity of the atoms yield a doppler shift of the imaging laser of approximately $0.86 \cdot \Gamma$. This effect leads to a wrong atom number estimation.

Suppose the atom number measurement is wrong by a constant factor $\alpha$. This yields that the estimated mean atom number and the estimated standard deviation of the atom number change:

$$N \to \alpha N \tag{5.27}$$

$$\langle N \rangle \to \alpha \langle N \rangle \tag{5.28}$$

$$\Delta N = \frac{1}{n-1}\sqrt{\sum_{i=1}^{n}(N_i - \langle N \rangle)^2} \to \alpha \Delta N \tag{5.29}$$

In the noise plot the ratio of the variance of the atom number measurement vs. the

mean atom number is plotted.

$$\frac{(\Delta N)^2}{\langle N \rangle} \rightarrow \alpha \frac{(\Delta N)^2}{\langle N \rangle} \tag{5.30}$$

This means an overestimation of the atom number would lead to a higher noise level. For our measurement plotted in fig. 5.8 an factor of $\alpha \approx 3 \pm 1$ would lead to an agreement of the measured data with the theory curve. Although approximately 90 measurements have been done for every depicted data point, the errorbars are still to big to give this factor more precise.

# Chapter 6

# Conclusion and Outlook

In our setup a double well system is used. This allows the measurement of thermal and quantum fluctuations. The measurement of the thermal fluctuations has already been achieved [39, 50, 51] in our system, but for a measurement of the quantum fluctuations the accessible parameter range of the system had to be expanded. Therefore the scope of this work was to introduce the new trapping beam (the charger). A short introduction to the two-mode model was given, which can be used to describe the dynamics in our double well system. Since the experimental conditions can be set such that only two wells are populated, it is relatively easy to deduce the phase between both lattice sites, compared to a setup that uses an optical lattice for instance. The relevant parameters for the dynamics of a Bose-Einstein condensate confined in a double well potential are charging energy $E_c$, which is a measure for the on-site interaction, and the Josephson tunneling energy $E_J$ which is an estimate of the coupling strength between the wells. The old setup consisting of the waveguide and the crossed dipole trap yielded a good control of $E_J$, but $E_c$ stayed always well below the tunneling coupling and even well below the typical temperature scale of the experiment. Hence the experiment was always limited to the Josephson regime, where $E_J \gg E_c \gg E_J/N^2$. To come into a regime where quantum fluctuations are observable both of them have to be increased at least to approximately the same value as the thermal energy scale. Therefore the confinement in each well has to be enhanced while still having control of the separating barrier height. With the old setup the only way to reach this would be increasing the optical power which would have also increased the scattering rate to a value where the condensate would be destroyed at a timescale too short for the experiment. This solution would also raise the temperature to a higher level, resulting in a higher value needed for $E_c$ to be comparable to the temperature. So a low power solution is favorable, which is to increase the confinement by decreasing the spot size of the trapping beam. This has been realized with the charger, which has a $1/e^2$ waist of $5.15\,\mu$m.

The properties of this beam have been discussed and a first measurement taking advance of the strong confinement has been done which is the study of the decay of a trapped thermal gas due to one and three-body losses. A theoretical description of the loss procedure was developed, starting from the rate equation formalism. From this a master equation was deduced and the problem was tackled using the approximation that the cloud's density has always a gaussian shape. The theoretical results are found to be in quite good agreement with the exact solution calculated at low atom numbers. It was also compared to a Monte-Carlo method of solving the rate equation and found to fit

well. Although the theoretical description predicts the uncertainty of the atom number in the trap to go below the shot noise limit, this could not be observed in the experiment.

# Outlook

Since this deviation from the theoretic behavior might also be a problem of the imaging system, a new setup using a new objective built as a diploma work by T. B. Ottenstein [52] is just installed. With this one should have a closer look to this loss measurements again and it should be possible to overcome the shot noise threshold in the atom number fluctuations. By doing the same in a double well potential with Bose condensed particles the three body loss could be used to prepare a number squeezed state as an input state to an BEC interferometer [58]. A squeezing in the atom number has already been observed by M. Greiner *et al.* [59] in an optical lattice, but has not yet been observed in a double well, where one would have a "pure" interferometer with only two paths.

Another goal would be to go towards the Fock regime and try to see quantum fluctuations. One effect would be the observation of phase diffusion and the revival of the phase in a double well potential [60, 61, 62]. The phase revival has already been observed in an optical lattice by M. Greiner *et al.* [63]. The optical lattice has two advances compared to a double well system which makes it "easy" to find the right evolution time: At first in a lattice only very few atoms can be loaded reliable in the system per lattice site. In the above mentioned experiments 1 to 3 atoms have been used in every lattice site. As a second point, in a double well system the contrast in a single interference picture is always high, independent of the randomness of the relative phase. Many shots have to be averaged to decide if the relative phase is fixed or completely random. In an optical lattice this information can be observed by one experimental realization. If the relative phase between the lattice sites is random no interference fringes will occur, since the averaging is done by the system itself. This averaging of the system is also the main disadvantage of the optical lattice in comparison to a double well system. At half the revival time of the relative phase, the system should be in a phase cat state [64]. This state is not observable in a lattice, as the mean phase is random. But this randomness is produced by only two discrete phases of $\pi/2$ and $-\pi/2$. This state is only observable in a double well system, where clear interference fringes are visible at every time of the experiment. It therefore allows the creation of a phase cat state of 500 to 1000 atoms.

# Appendix A

# *MatLab* code for rolling dice method

The following code was written in *MatLab* to calculate the one and three-body loss rate of a sample of atoms in a trap. This code uses the *Monte Carlo* approach, by rolling a dice for one and three-body collisions respectively as mentioned in section 5.1.2 on page 37.

Since *MatLab* is not very fast in computing loops the computation was rewritten as a *C* program, which is called by *MatLab* to give the necessary parameters.

As the method in the *C* and *MatLab* programs are the same, only the *MatLab* code is shown here.

```
% some necessary inputs
K1 = double(0.1);    % one-body loss rate
K3 = double(1e-6);   % three-body loss rate
N0 = 100;            % initial atom number
tmax = 10;           % calculate up to tmax seconds
loop = 1000;         % number of runs to calculate the decay
w = 2.5;             % initial shot noise level

n=[]; dt=[]; m=[]; N=[]; t = []; Natom = []; Natm = [];

% calculate time step

dt = min(1e-3/K1,1e-3/(K3*N0^2));


for v=1:loop
    Nrand = round(N0+w*sqrt(N0)*randn(1));
    if Nrand<0 Nrand=0; end
    Natm = Nrand;

% roll the dice for loosing all the atoms once

    for u=1:(tmax/dt)

% one body losses

        l= rand(1,Nrand);
        n(l<=K1*dt)=1;
```

```
% three body losses

        l= rand(1,Nrand);
        m(l<=K3/3*(Nrand-1)*(Nrand-2)*dt)=3;

% calculate new atom number

        Nrand = Nrand-sum(n)-sum(m);
        if Nrand<0 Nrand=0; end
        Natm = [Natm Nrand];
        n = []; m=[]; l=[];

    end

    N = [N ; Natm];

% display the improvement of the calculation

    disp(['progess noiselevel: ' num2str(w) ' is now: '
       num2str(v/loop*100) '%'])

end

% create time step vector

t = dt:dt:dt*size(N,2);

% calculate mean value and standard deviation

Nav = mean(N);
stdN = std(N);
```

# Bibliography


[1] The Royal Swedish Academy of Sciences. The Nobel Prize in Physics 2001, 2001.

[2] S. N. Bose. Plancks Gesetz und Lichtquantenhypothese. *Z. Phys.*, **24**:178, 1924.

[3] A. Einstein. Quantentheorie des einatomigen idealen Gases. *Sitzungsberichte der Königlich-Preußischen Akademie der Wissenschaften*, **1**:3, 1925.

[4] J. F. Allen and A. D. Misener. Flow of Liquid Helium II. *Nature*, **141**:75, 1938.

[5] P. Kapitza. Viscosity of Liquid Helium below the $\lambda$-Point. *Nature*, **141**:74, 1938.

[6] F. London. The $\lambda$-Phenomenon of Liquid Helium and the Bose-Einstein Degeneracy. *Nature*, **141**:643, 1938.

[7] F. London. On the Bose-Einstein Condensation. *Physical Review*, **54**:947, 1938.

[8] L .Tisza. Transport Phenomena in Helium II. *Nature*, **141**:913, 1938.

[9] L. Landau. Theory of the Superfluidity of Helium II. *Physical Review*, **60**:356, 1941.

[10] M. H. Anderson, J. R. Ensher, M. R. Matthews, C. E. Wieman, and E. A. Cornell. Observation of Bose-Einstein Condensation in a Dilute Atomic Vapor. *Science*, **269**:198, 1995.

[11] K. B. Davis, M.-O. Mewes, M. R. Andrews, N. J. van Druten, D. S. Durfee, D. M. Kurn, and W. Ketterle. Bose-Einstein Condensation in a Gas of Sodium Atoms. *Physical Review Letters*, **75**:3969, 1995.

[12] C. C. Bradley, C. A. Sackett, J. J. Tollett, and R. G. Hulet. Evidence of Bose-Einstein Condensation in an Atomic Gas with Attractive Interactions. *Physical Review Letters*, **75**:1687, 1995.

[13] D. G. Fried, T. C. Killian, L. Willmann, D. Landhuis, S. C. Moss, D. Kleppner, and T. J. Greytak. Bose-Einstein Condensation of Atomic Hydrogen. *Physical Review Letters*, **81**:3811, 1998.

[14] M. R. Andrews, C. G. Townsend, H.-J. Miesner, D. S. Durfee, D. M. Kurn, and W. Ketterle. Observation of Interference Between Two Bose Condensates. *Science*, **275**:637, 1997.

[15] J. C. Davis and R. E. Packard. Superfluid $^3$He Josephson weak links. *Review of Modern Physics*, **74**:741, 2002.

[16] B. D. Josephson. Possible new Effects in Superconductive Tunneling. *Physics Letters*, **1**:251, 1962.

[17] P. W. Anderson and J. M. Rowell. Probable Observation of the Josephson Superconducting Tunneling Effect. *Physical Review Letters*, **10**:230, 1963.

[18] M. Albiez, R. Gati, J. Fölling, S. Hunsmann, M. Cristiani, and M. K. Oberhtaler. Direct Observation of Tunneling and Nonlinear Self-Trapping in a single Bosonic Josephson Junction. *Physical Review Letters*, **95**:010402, 2005.

[19] L. de Broglie. A Tentative Theory of Light Quanta. *Phil. Mag.*, **47**:446, 1924.

[20] C. Davisson and L. H. Germer. Diffraction of Electrons by a Crystal of Nickel. *Physical Review*, **30**:705, 1927.

[21] V. Giovannetti, S. Lloyd, and L. Maccone. Quantum-Enhanced Measurements: Beating the Standard Quantum Limit. *Science*, **306**:1330, 2004.

[22] Marlan O. Scully and Jonathan P. Dowling. Quantum-noise limits to matter-wave interferometry. *Physical Review A*, **48**:3186, 1993.

[23] Marlan O. Scully and M. Suhail Zubairy. Quantum Optics. Cambridge University Press, Cambridge, 2006.

[24] J. A. Dunningham, K. Burnett, and S. Barnett. Interferometry below the Standard Qunatum Limit with Bose-Einstein Condensates. *Physical Review Letters*, **89**:150401, 2002.

[25] B. Yurke. Input States for Enhancement of Fermion Interferometer Sensitivity. *Physical Review Letters*, **56**:1515, 1986.

[26] J. Javanainen and M. Y. Ivanov. Splitting a trap containing a Bose-Einstein condensate: Atom number fluctuations. *Physical Review A*, **60**:2351, 1999.

[27] Y. Castin and J. Dalibard. Relative phase of two Bose-Einstein condensates. *Physical Review A*, **55**:4330, 1997.

[28] D. Ananikian and T. Bergeman. Gross-Pitaevskii equation for Bose particels in a double-well potential: Two-mode models and beyond. *Physical Review A*, **73**:013604, 2006.

[29] Michael Albiez. Observation of nonlinear tunneling of a Bose-Einstein condensate in a single Josephson junction. PHD thesis, University of Heidelberg, 2005.

[30] Thomas Anker. Ultracold quantum gases in one-dimensional optical lattice potentials - nonlinear matter wave dynamics -. PHD thesis, University of Heidelberg, 2005.

[31] Jonas Fölling. Bose-Einstein Josephson Tunneling and Generation of Arbitrary Optical Potentials. Diploma thesis, University of Heidelberg, 2005.

[32] Börge Hemmerling. Thermally Induced Fluctuations in a Bosonic Josephson Junction. Diploma thesis, University of Heidelberg, 2006.

[33] Anthony J. Leggett. Bose-Einstein condensation in the alkali gases: Some fundamental concepts. *Reviews of Modern Physics*, **73**:307–356, 2001.

[34] S. Raghavan, A. Smerzi, S. Fantoni, and S.R. Shenoy. Coherent oscillations between two weakly coupled Bose-Einstein condensates: Josephson effects, $\pi$ oscillations, and macroscopic quantum self-trapping. *Physical Review A*, **59**(1):620–633, 1999.

[35] E. P. Gross. Structure of a Quantized Vortex in Boson Systems. *Nuovo Cimento*, **20**:45, 1961.

[36] E. P. Gross. Hydrodynamics of a Superfluid Condensate. *Journal of Mathematical Physics*, **4**:195, 1963.

[37] L. P. Pitaevskii. Vortex Lines in an Imperfect Bose Gas. *Sov. Phys. JETP*, **13**:451, 1961.

[38] G.-S. Paraoanu, S. Kohler, F. Sols, and A.J. Leggett. The Josephson plasmon as a Bogoliubov quasiparticle. *Journal of Physics B: Atomic, Molecular and Optical Physics*, **34**:4689–4696, 2001.

[39] Rudolf Gati. Bose-Einstein Condensates in a single Double Well Potential. PHD thesis, University of Heidelberg, 2007.

[40] Paul L. DeVries. Application of the Split Operator Fourier Transform method to the solution of the nonlinear Schrödinger equation. *AIP Conference Proceedings*, **160**:269, 1987.

[41] J. C. Mather, D. J. Fixsen, R. A. Shafer, C. Mosier, and D. T. Wilkinson. Calibrator Design for the *COBE* Far-Infrared Absolute Spectrometer (FIRAS). *The Astrophysical Journal*, **512**:511–520, 1999.

[42] Bernd Eiermann. Kohärente nichtlineare Materiewellendynamik - Helle atomare Solitonen -. PHD thesis, University of Konstanz, 2004.

[43] Stefan Hunsmann. Josephson-Effekte in Bose-Einstein Kondensaten. Diploma thesis, University of Heidelberg, 2004.

[44] Matthias Taglieber. Helle atomare Gap-Solitonen. Diploma thesis, University of Konstanz, 2003.

[45] K. Dieckmann, R. J. C. Spreeuw, M. Weidemüller, and J. T. M. Walraven. Two-dimensional magneto optical trap as a source of slow atoms. *Physical Review A*, **58**(5):3891, 1998.

[46] High Density Atomic Beam Atom Funnel for the Production of a Slow. Erling Riis and David S. Weis and Kathryn A. Moler and Steven Chu. *Physical Review Letters*, **64**:1658, 1990.

[47] E. L. Raab, M. Prentiss, Alex Cable, Steven Chu, and D. E. Pritchard. Trapping of Neutral Sodium Atoms with Radiation Pressure. *Physical Review Letters*, **59**:2631, 1987.

[48] Wolfgang Petrich, Michael H. Anderson, Jason R. Ensher, and Eric A. Cornell. Stable, Tightly Confining Magnetic Trap for Evaporative Cooling of Neutral Atoms. *Physical Review Letters*, **74**:3352, 1995.

[49] Harold J. Metcalf and Peter van der Straten. Laser Cooling and Trapping. Springer, New York, 1999.

[50] R. Gati, B. Hemmerling, J. Fölling, M. Albiez, and M. K. Oberthaler. Noise Thermometry with Two Weakly Coupled Bose-Einstein Condensates. *Physical Review Letters*, **96**:130404, 2006.

[51] R. Gati, J. Esteve, B. Hemmerling, T. B. Ottenstein, J. Appmeier, A. Weller, and M. K. Oberthaler. A primary noise thermometer for ultracold bose gases. *New Journal of Physics*, **8**:189, 2006.

[52] Timo Bastian Ottenstein. A New Objective for High Resolution Imaging of Bose-Einstein Condensates. Diploma thesis, University of Heidelberg, 2006.

[53] Lev Pitaevskii and Sandro Stringari. Bose-Einstein Condensation. Oxford Science Publications, Oxford, 2003.

[54] E. A. Burt, R. W. Ghrist, C. J. Myatt, M. J. Holland, E. A. Cornell, and C. E. Wieman. Coherence, Correlations, and Collisions: What One Learns about Bose-Einstein Condensates from Their Decay. *Physical Review Letters*, **79**(3):337, 1997.

[55] J. Söding, D. Guéry-Odelin, P. Desbiolles, F. Chevy, H. Inamori, and J. Dalibard. Three-body decay of a rubidium Bose-Einstein condensate. *Applied Physics B: Lasers and Optics*, **69**:257–261, 1999.

[56] P. S. Julienne, F. H. Mies, E. Tiesinga, and C. J. Williams. Collisional Stability of Double Bose Condensates. *Physical Review Letters*, **78**:1880, 1997.

[57] Tino Weber, Jens Herbig, Michael Mark, Hanns-Christoph Nägerl, and Rudolf Grimm. Three-Body Recombination at Large Scattering Lengths in an Ultracold Atomic Gas. *Physical Review Letters*, **91**:123201, 2003.

[58] Carlton M. Caves. Quantum-mechanical noise in an interferometer. *Physical Review D*, **23**:1693, 1981.

[59] M. Greiner, O. Mandel, T. Esslinger, T. W. Hänsch, and I. Bloch. Quantum phase transition from a superfluid to a Mott insulator in a gas of ultracold atoms. *Nature*, **415**:39, 2002.

[60] M. Lewenstein and L. You. Quantum Phase Diffusion of a Bose-Einstein Condensate. *Physical Review Letters*, **77**:3489, 1996.

[61] A. Imamoglu, M. Lewenstein, and L. You. Inhibition of Coherence in Trapped Bose-Einstein Condensates. *Physical Review Letters*, **78**:2511, 1997.

[62] Augusto Smerzi and Srikanth Raghavan. Macroscopic quantum fluctuations in the Josephson dynamics of two weakly linked Boes-Einstein condensates. *Physical Review A*, **61**:063601, 2000.

[63] Markus Greiner, Olaf Mandel, Theodor W. Hänsch, and Immanuel Bloch. Collapse and revival of the matter wave field of a BoseEinstein condensate. *Nature*, **419**:51, 2002.

[64] V. Bužek, H. Moya-Cessa, P. L. Knight, and S. J. D. Phoenix. Schrödinger-cat states in the resonant Jaynes-Cummings model: Collapse and revival of oscillations of the photon-number distribution. *Physical Review A*, **45**:8190, 1992.

# Danksagung

An dieser Stelle möchte ich mich bei allen bedanken, die mich während meines Studiums und der Diplomarbeit unterstützt haben:

- Zu allererst möchte ich mich bei meinem Betreuer Prof. Dr. Markus K. Oberthaler für die Chance bedanken in seiner Gruppe mit zu arbeiten. Seine offene Art, seine Begeistung für die Physik und Pizza Diabolo und sein unermüdlicher Einsatz für seine Gruppe haben entscheidend zum gelingen dieser Arbeit beigetragen. Auch möchte ich ihm für sein unerschütterliches Vertrauen in meine Fähigkeiten danken.

- Ich möchte Juniorprof. Dr. Selim Jochim für die Begutachtung meiner Arbeit danken. Ich wünsche ihm und seinem Team um Timo Ottenstein viel Erfolg bei ihrem Projekt.

- „Meinem "Labor um Jérôme Estève, Rudolf Gati, Andreas Weller, Christian Gross, Timo Ottenstein (jetzt am MPI für Kernphysik) und Tilman Zibold möchte ich für die sehr gute Zusammenarbeit, die lockere Atmosphäre und den ganzen Spaß, den wir gemeinsam hatten danken. Ich habe viel von euch lernen können und habe die Zeit im Labor immer genossen.

- Dem Rest der Gruppe mit Lisa Kierig, Ute Schnorrberger (die uns in Richtung Mainz verlasen hat), Karsten Joho, Arne Schietinger, Joachim Welte und Jirka Tomkovic sowie dem neuen (und meinem neuen) Labor um Marc Repp, Stefan Weis und Jan Krieger danke ich für die angenehme Atmosphäre in und außerhalb des Instituts und den guten Zusammenhalt in der Gruppe.

- Ein ganz besonderer Dank gilt meinen Eltern Werner und Marion Appmeier, die mich immer unterstützt haben und mir so das Studium erst ermöglicht haben.

- Ich möchte an dieser Stelle meiner Lebensgefährtin Donata Danzmann für die wunderbare Zeit mit Ihr danken. Du warst immer für mich da. Du bist mein bester Freund, mein größter Fan und mein härtester Kritiker. Ich liebe Dich.

Erklärung:

Ich versichere, dass ich diese Arbeit selbstständig verfasst und keine anderen als die angegebenen Quellen und Hilfsmittel benutzt habe.

Heidelberg, den _____ _____

Unterschrift